Revised version

UV/Vis Single-Crystal Spectroscopic Investigation of Almandine-Pyrope and Almandine-Spessartine Solid Solutions: Part I. Spin-Forbidden $Fe^{2+,3+}$ and Mn^{2+} Electronic-Transition Energies, Crystal Chemistry and Bonding Behavior

Charles A. Geiger[1,*], Michail N. Taran[2], and George R. Rossman[3]

[1] Department of Chemistry and Physics of Materials
University of Salzburg
Jakob Haringer Str. 2a
A-5020 Salzburg, Austria

[2] M.P. Semenenko Institute of Geochemistry and Mineralogy and Ore Formation
National Academy of Sciences of Ukraine
Palladin Ave. 34
03142 Kyiv-142, Ukraine

[3] Division of Geological and Planetary Sciences
California Institute of Technology
Pasadena, CA, 91125-2500, USA

[*]Corresponding author
Fax: ++43-662-8044-6289
Tel.: ++43-662-8044-6226
E-mail: ca.geiger@plus.ac.at

Written using a Macintosh with Word 16.16.3

Date: 01.06.2022

This is the peer-reviewed, final accepted version for American Mineralogist, published by the Mineralogical Society of America.
The published version is subject to change. Cite as Authors (Year) Title. American Mineralogist, in press.
DOI: https://doi.org/10.2138/am-2022-8499. http://www.minsocam.org/

ABSTRACT

Aluminosilicate garnet is an excellent phase to research solid-solution behavior in silicates. Natural almandine-pyrope, $\{Fe^{2+}_{3x},Mg_{3-3x}\}[Al_2](Si_3)O_{12}$, and almandine-spessartine, $\{Fe^{2+}_{3x},Mn^{2+}_{3-3x}\}[Al_2](Si_3)O_{12}$, crystals were measured by UV/Vis/NIR (~29000 to 10000 cm^{-1}) optical absorption spectroscopy using a microscope. The spectra and changes in energy of a number of Fe^{2+} and Mn^{2+} spin-forbidden electronic transitions of different wavenumber were analyzed as a function of garnet composition across both binaries. The spectra of Alm-Pyp garnets are complex and show a number of Fe^{2+} and Fe^{3+} transitions manifested as overlapping absorption bands whose intensities depend on composition. There are differences in energy behavior for the various electronic transitions, whereby lower wavenumber Fe^{2+} transitions decrease slightly in energy with increasing pyrope component and those of higher wavenumber increase. The spectra of Alm-Sps solid solutions show both Fe^{2+} and Mn^{2+} spin-forbidden bands depending upon the garnet composition. The variations in energy of the different wavenumber Fe^{2+} transitions are unlike those observed in Alm-Pyp garnets. The three lowest wavenumber electronic transitions appear to vary the most in energy across the Alm-Sps join compared to those at higher wavenumber. Four narrow and relatively intense Mn^{2+} spin-forbidden bands between 23000 and 25000 cm^{-1} can be observed in many Sps-Alm garnets. Their transition energies may increase or decrease across the join, but scatter in the data prohibits an unequivocal determination. A consistent crystal-chemical model and Fe^{2+}-O bond behavior, based on published diffraction and spectroscopic results, can be constructed for the Alm-Pyp binary but not for the Alm-Sps system. The spectra of the former garnets often show the presence of high wavenumber spin-forbidden bands that can be assigned to electronic transitions of Fe^{3+} occurring at the octahedral site. The most prominent band lies between 27100 and 27500 cm^{-1} depending on the garnet composition. Fe^{3+}-O^{2-} bonding is analyzed using Racah parameters. State-of-the-art electronic structure calculations are needed to understand the precise physical nature of the electronic transitions in garnet and to interpret better UV/Vis/NIR spectra.

Keywords: UV/Vis/NIR spectroscopy, garnet, solid solutions, electronic spin-forbidden transitions, crystal chemistry.

INTRODUCTION

Aluminosilicate garnet, general formula $\{X_3\}[Al_2](Si_3)O_{12}$, where X = Mg, Fe^{2+}, Mn^{2+} and Ca, is a key rock-forming mineral occurring in different geologic settings. Many upper-mantle and some crustal garnets are largely pyrope-almandine solid solutions, $\{Mg_{3x}Fe^{2+}_{3-3x}\}[Al_2](Si_3)O_{12}$, and spessartine-almandine garnets, $\{Mn^{2+}_{3x}Fe^{2+}_{3-3x}\}[Al_2](Si_3)O_{12}$, occur in certain crustal granites and pegmatites. Atomic mixing at {X} can be complete for both binaries as shown by compositional analyses of natural garnets (Boeke 1914; Sobolev 1964) and the successful laboratory synthesis of crystals along both joins at elevated pressures and temperatures (e.g., Geiger and Feenstra 1997).

Investigation of the solid-solution behavior of aluminosilicate garnets, both at the micro and macroscopic scale, is a long, continuing work in progress (Geiger 2008, 2016) and much still needs to be researched. A fundamental problem is in trying to understand the nature of local structural heterogeneity that arises through the exchange of different atoms of varying sizes and electronic properties. Local X^{2+}-O chemical bonds must vary slightly as a function of crystal composition. Garnet is an excellent phase to study solid solutions, because Fe^{2+}, Mg and Mn^{2+} mix at the single crystallographic {X} site. All three cations have relatively similar ionic radii, but Mg does not have *d* electrons unlike Fe^{2+} ($3d^6$) and Mn^{2+} ($3d^5$). The chemical-bonding behavior of the latter two transition metals with oxygen should differ between each other and both most certainly with respect to the alkaline Mg cation. A notable crystal-chemical feature of the aluminosilicate garnets is the anisotropic vibrational behavior of the different X^{2+} cations and their probable anharmonic potentials (Geiger 2013). In order to understand a wide range of atomic-scale and bonding behavior in crystals various spectroscopic measurements are necessary (Geiger 2004).

Optical absorption spectroscopy is a powerful tool for investigating the electronic states of atoms and chemical-bonding behavior. There have been a number of studies made on different aluminosilicate garnets relating to the electronic absorption bands arising from different transition metals in their various oxidation states, as recorded in the UV/Vis/NIR spectral regions (e.g., Clarke 1957; Manning 1967, 1972; Slack and Chrenko 1971; Moore and White 1972; White and Moore 1972; Runciman and Sengupta 1974; Runciman and Marshall 1975; Smith and Langer 1983; Geiger and Rossman 1994; Geiger et al. 2000; Taran et al. 2002; Khomenko et al. 2002; Taran et al. 2007; Krambrock et al. 2013; Platonov and Taran 2018). The spin-allowed electronic transitions of Fe^{2+} for a series of almandine-pyrope and almandine-spessartine solid solutions in the near infrared (NIR) region have been measured and an analysis made using crystal field theory (Geiger and Rossman 1994). Taran et al. (Part II) measured the UV/Vis spectra of two different composition almandine bearing and several spessartine-rich garnets and analyzed the spin-forbidden electronic transitions of Fe^{2+} and Mn^{2+}, respectively.

Crystal field theory, though a simple physical model, has proved useful in studying crystals with ionic bonding (Burns 1970, 1993). Electronic transitions, both spin-allowed and spin-forbidden, of cations are often interpreted and assigned using theoretical Tanabe-Sugano diagrams that consider cubic, O_h, symmetry. The diagrams indicate that the energies of spin-allowed transitions of Fe^{2+}, for example, vary much more as a function of local Fe^{2+}-O bond lengths (i.e., Dq) in different garnet compositions (see Geiger and Rossman 1994) compared to Fe^{2+} spin-forbidden transitions. Indeed, based on theory, most Fe^{2+} and Mn^{2+} spin-forbidden transition energies should be largely independent of garnet composition. However, this has not been investigated and tested experimentally over a range of garnet compositions, for example, across a binary solid solution. In other words, it has not been studied to what degree, if any, the various electronic energies can vary as a function of garnet composition. And if they do, it needs to be determined if they could give information on local cation coordination environments (i.e., Fe^{2+}-O and Mn^{2+}-O bonding) in a structurally heterogeneous solid solution (see Bosenick et al.

2000; Freeman et al. 2006). In addition, it is not known from theory how spin-forbidden Fe^{2+} and Mn^{2+} transition energies behave under point symmetry D_2, as in the triangular dodecahedron of the garnet structure. Semi-empirical calculations of Fe^{2+} transition energies, beyond the level given by simple crystal field and Tanabe-Sugano theory, for garnet are contradictory (i.e., Guo-Yin and Min-Guang 1984; Zhou and Zhao 1984). They also are not in good and full agreement with experimental spectra (Taran et al. - Part II). The nature of Mn^{2+} transition energies is even more poorly understood.

Geiger et al. (2003) undertook ab-initio cluster-based electronic-structure calculations to obtain the energies and interpret the spin-allowed Fe^{2+} transitions for various aluminosilicate garnets including binary solid solutions. We are not aware of any recent theoretical or computational studies that give information on spin-forbidden Fe^{2+} and Mn^{2+} transitions and related chemical-bonding properties. In order for calculations to be effective, the existing experimental database (i.e., spectroscopic) has to be as extensive and quantitative as possible. This is presently not the case for most silicate solid-solution systems, and, here, specifically garnet. Thus, careful experimental measurements of spin-forbidden Fe^{2+} and Mn^{2+} energies for a compositionally well-defined binary garnet solid solution are clearly needed.

Considering the various issues, we investigate using UV/Vis single-crystal absorption spectroscopy, the energies of different electronic spin-forbidden bands associated with Fe^{2+} in natural, closely binary almandine-pyrope and Fe^{2+} and Mn^{2+} in natural binary almandine-spessartine solid solutions. The role of Fe^{3+}, in nominally Fe^{3+}-free almandine-pyrope garnets, is also studied. The electronic energies of spin-forbidden transitions, local crystal-chemical properties and first-order bonding behavior are considered and conclusions drawn.

SAMPLES AND EXPERIMENTAL METHODS: CRYSTALS USED FOR STUDY AND UV/Vis SPETROSCOPY

Samples

The garnets used in this study (as well as for other upcoming works as part of this broad spectroscopic investigation on garnet) from the collections of CAG, MNT, and GRR. Almandine-pyrope garnets are described in Table 1a and almandine-spessartine garnets in Table 1b. The crystals did not show any large deviations from isotropic behavior. The various single crystals, adopted for measurement, were carefully prepared as doubly polished single-crystal platelets of varying thicknesses for spectroscopic and EDS microprobe measurements. Care was used to obtain the necessary crystal thicknesses in order to record all types of electronic transitions correctly. The garnets, depending on their origin, can have various inclusions, cracks and other "defects", which can complicate the UV/Vis measurements. They can, for example, affect significantly the absorption background of a spectrum through the scattering of light. Clean and transparent areas were selected for study when possible.

UV/VIS optical absorption single-crystal spectroscopy

In Pasadena, spectra in the wavelength (wavenumber) range between about 380 nm (26400 cm^{-1}) to 1050 nm (9500 cm^{-1}) were obtained at about 1.5 nm resolution with a homebuilt microspectrometer. The device contains a 1024 element Si diode-array detector coupled to a 1/3-meter grating spectrometer system attached via fiber optics to a highly modified NicPlan infrared microscope. A few spectra were obtained with an older Cary 17I spectrometer system operating at about 1.4 nm resolution that included a photomultiplier tube for the UV/Vis region and a PbS detector for NIR work. Optical spectra were recorded at room temperature and were typically taken on a square area 0.4 to 0.5 mm on a side from a larger crystal.

In Kyiv, spectra were recorded at room temperature using a self-made single-beam microspectrophotometer. It is constructed from a SpectraPro-275 triple grating monochromator and a modified mineralogical microscope, MIN-8, and a PC. Two Ultrafluars 10x objectives served as the objective and condenser in the microscope. The measuring spot was not larger than 200 µm. Two photomultiplier tubes and a PbS cell, cooled by the Peltier effect down to -20 °C,

were used as interchangeable photodetectors. The presence of a mechanical high-stability 300 Hz-chopper and lock-in amplifier improve the signal/noise ratio in the 1000-1800 nm (10000-5556 cm^{-1}) range. Stable xenon and quartz-halogen lamps, both with 70 W power, were used as light sources in the ranges 330-450 nm (30303-22222 cm^{-1}) and 450-1800 nm (22222-5556 cm^{-1}), respectively. The spectra were scanned at steps of $\Delta\lambda$ = 1 nm, 2 nm and 5 nm in the range 330-450 nm (30303-22222 cm^{-1}), 450-1000 nm (22222-10000 cm^{-1}) and 1000-1800 nm (10000-5556 cm^{-1}), respectively. This was done by means of a digital wavelength-step-scanning procedure with an Acton Research Corporation SpectaCard readout system driven by Windows SC-1 control and data-acquisition software.

Band wavenumbers were determined visually by taking the energy at maximum absorption. For the setup in Kiev, we estimate the uncertainty in the Vis region to be around ± 25 cm^{-1} in the case of narrow and well-resolved absorption features. The uncertainty in the energy of weak and broad bands, as well as those that appear as shoulders, is larger. In the UV region, the uncertainty in band energies should also be a little greater.

Composition determinations

The chemical composition of the different garnets was determined by WDS electron microprobe or single-crystal XRF analysis at Caltech or using a field-emission scanning electron microscope, model JSM-6700F, equipped with an energy-dispersive spectrometer (EDS), model JED-2300, at the Semenenko Institute in Kiev. The analyses with the latter were made on carbon-coated garnet platelets that were used for the spectroscopic measurements. The operating conditions were 15 kV accelerating voltage, 0.75 nA beam current, 1 μm beam size and a counting time of 60 seconds for each point analysis. Elemental Si, Ti, Al, Cr, Fe, Mn and synthetic MgO and CaF_2 were used as standards. The measured raw counts were corrected for matrix effects with the ZAF algorithm implemented by JEOL. Five to seven spots were analyzed per crystal and were averaged to obtain the final composition.

RESULTS

The chemical analyses showed that the crystals were largely compositionally homogeneous and they did not show any major zoning. The crystal-chemical formulas of the studied garnets are given in Tables 1a and 1b. The various recorded garnet UV/Vis spectra will be shown in the course of the discussion section. However, first, a short interlude into crystal field theory and electronic transitions will be made. The purpose of this is to provide a short theoretical background for this study of Fe^{2+} and Mn^{2+} spin-forbidden transitions for binary almandine-pyrope and almandine-spessartine solid solutions. Our second accompanying work (Taran et al. Part II) involves an analysis on the number, intensities and assignments of Fe^{2+} spin-forbidden transitions in one almandine and one pyrope garnet and Mn^{2+} in a number of different composition spessartine-rich garnets. A third investigation (Geiger and Taran Part III) considers metal-metal intervalence, i.e., $Fe^{2+} + Fe^{3+} \rightarrow Fe^{3+} + Fe^{2+}$, charge transfer transition for garnets in the system almandine-pyrope-spessartine-grossular. The nature of ligand-metal charge transfer is also discussed in part in Parts II and III.

DISCUSSION

Light absorption, electronic interactions and UV/Vis spectra of transition-metal-bearing crystals

Optical absorption spectra of minerals containing $3d^N$ transition-metal ions, where N is the number of *d* electrons, can show electronic absorption bands of three main types. They can occur in the UV, Vis, and NIR spectral regions. They are: (i) crystal-field or *dd*-transition bands, (ii) charge-transfer bands of the ligand-metal and metal-metal type and (iii) bands of exchange-coupled $3d^N$-ion pairs. We discuss them briefly. A more complete treatment can be found in Marfunin (1979) and Burns (1970; 1993).

Crystal-field or *d-d* electronic transitions. They are frequently observed in the spectra of minerals and have received much study, both experimental and theoretical. They are caused by

electronic transitions between partly filled *d* orbitals of transition metal ions and they are often interpreted using crystal field theory (e.g., Marfunin 1979; Burns 1970; 1993). This theory describes the electronic interactions in a chromophore complex, for example, consisting of a central transition metal ion and the nearest surrounding ligands. The interaction between the negatively charged ligands and the positively charged central atom is assumed to be purely electrostatic. The metal atom resides in an electric field of a certain intensity and symmetry as caused by the nearest surrounding ligands whose precise electronic structure is ignored. The latter are regarded as structure-less point charges (or sometimes as dipoles) having an outer electrostatic field. The crystal field strength, *Dq*, of a metal-ligand bond is given by:

$$10Dq = \frac{5\langle r^4\rangle(Z_L e^2)}{3\bar{R}^5} \quad (1),$$

where $\bar{R}$ is the mean metal-ligand distance, $\langle r^4\rangle$ is mean value to the fourth power of the radial distance of a 3*d* orbital from the nucleus, and $(Z_L e^2)$ is the charge on the ligands. The numerator is assumed to be approximately constant for cations of similar valence within the same transition series. With increasing *R*, the influence of other ions not belonging to the main coordination polyhedron is considered small and in most cases is neglected.

The ligand field acting on a central ion causes a splitting of the electronic energy levels of the $3d^N$ ion, which are degenerate in the free spherically symmetrical state. The splitting is a function of the degree of deviation of the local symmetry from a spherical one due to the immediate surrounding crystal field. Electronic transitions from the lowest energy level (i.e., the ground state) to higher energy levels (i.e., excited states) result from the absorption of a quantum of electromagnetic radiation of a given energy. The energy of a transition is given by a band in an experimental optical absorption spectrum. Thus, optical spectra give information on the electronic structure of a $3d^N$ ion in a local crystal field.

In accordance with Hund's rule, the ground electronic state has the largest spin multiplicity, *S*, for a given $3d^N$ electronic configuration. There are spin-allowed (i.e., $\Delta S = 0$)

and/or spin-forbidden (i.e., $\Delta S \neq 0$) transitions depending on the difference in spin multiplicities of the electronic states involved in a transition. The former bands are typically broad and intense with an oscillator strength of $f = 10^{-4}$ to 10^{-5}. The latter are three to four orders of magnitude weaker and tend to be narrow in breadth. They can occur on or overlap other more intense electronic bands. The energy and broadness of both spin-allowed and spin-forbidden bands can be analyzed using Tanabe-Sugano diagrams in the approximation of local cubic symmetry, namely O_h (e.g., Burns 1993). In the case of lower symmetry, as is typical for many mineral structures, degenerate electronic levels split further. Here, Tanabe-Sugano diagrams are more difficult to apply and the interpretation of the spectra can be considerably more complicated (see Taran et al. Part II, for the case of spessartine).

It should be noted that crystal field theory (CFT) is incomplete in the sense that it treats the ligands surrounding a metal cation as simple point charges. Covalent bonding properties are not accounted for as in ligand field theory. Only the *d* orbitals of the metals are considered and not those of the *s* and *p* orbitals or the orbitals of the ligands. In terms of silicates, CFT has, though, been used successfully, because the bonding between transition metals and oxygen is largely ionic. Charge-transfer transitions, as discussed next, are also not treated by CFT.

Charge-transfer transitions. They can affect color, pleochroism and other spectroscopic properties of $3d^N$-ion-bearing minerals. They are subdivided into two different types: charge-transfer (CT) ligand-metal (L $\rightarrow$ M) and metal-metal (M $\rightarrow$ M) electronic transitions. The absorption bands related to the former are governed by Laporte or parity selection rules between bonding and anti-bonding molecular orbitals in a transition-metal-ligand coordination cluster, for example. The molecular orbitals are localized on the different atoms, both ligands and the central cation, and the electronic transitions are accompanied by a transfer of charge from the former to the latter. Because the L $\rightarrow$ M charge-transfer transition is allowed by parity selection rules, they are extremely intense with values of $f = 1$ to 10^{-1}. Their spectroscopic band maxima are typically

located in the high energy UV range of the electromagnetic spectrum. They are manifested in a typical optical absorption spectrum by their low energy absorption edge or flank that can extend down into the visible range. Thereby, color can be affected. Because L → M charge-transfer bands are so intense (i.e., their bands are difficult to record on scale) and because they occur mostly in the UV region, they have received little study in minerals.

Electronic M → M CT transitions can appear in the spectra of various oxides and silicates containing $3d^N$ ions that have different formal valence states. For example, minerals containing Fe^{2+} and Fe^{3+} can display intense coloration. The interaction involves the transfer of electronic density from the donor (e.g., Fe^{2+}) to the acceptor (e.g., Fe^{3+}) and it leads to electronic delocalization. In a number of Fe^{2+}- and Fe^{3+}-bearing oxides and silicates, for example, this interaction can give rise to a broad intense band between ~11,000 and ~18,000 cm^{-1}. In garnet, this type of transition occurs at higher energies around 21000-22000 cm^{-1} (Taran et al. 2007; Geiger and Taran Part III). In anisotropic crystals, these bands are polarized and they give rise to pleochroism. Heteronuclear IVCT transitions ($Fe^{2+} + Ti^{4+} \rightarrow Fe^{3+} + Ti^{3+}$) can also occur and their broad intense absorption bands typically lie at higher energies between 20,000 and 24,000 cm^{-1}.

Exchange-coupled transitions related to local pairing of $3d^N$ ions. An electronic exchange interaction between $3d^N$ ions may not necessarily lead to IVCT absorption bands in UV/Vis spectra, but it can cause an increase in the intensity of both spin-allowed and spin-forbidden crystal-field transitions.

Almandine and spessartine crystal chemistry

The garnet crystal structure is shown in Figure 1a. Local structural relationships between neighboring octahedra and dodecahedra, which contain transitions metals (i.e., for aluminosilicate garnets), are illustrated as well (Figures 1b, c and d). Common rock-forming

298 garnet can contain $Fe^{2+,3+}$, Cr^{3+}, $Mn^{2+,3+}$, V^{3+} and Ti^{4+} at major to minor concentrations depending
299 on the garnet species and the petrologic occurrence.

300 Most almandines contain (aside from Fe^{2+}), in general, major to minor Mn^{2+}, minor Fe^{3+}
301 and Ti^{4+} (Deer et al. 1982), while Mn^{3+}, Cr^{3+} and V^{3+} range from being minor to trace in
302 concentration. Cr concentrations between about 30 and 1000 ppm were measured for
303 compositionally zoned garnets from pelitic schists, for example, by Schwandt et al. (1996). V
304 concentrations were roughly between about 15 and 1000 ppm. Hickmott et al. (1987) measured
305 roughly 300 ppm Cr and much less V in a garnet from an amphibolite from the Tauern Window,
306 Austria. Copjaková et al. (2005) measured Cr and V concentrations mostly below 250 ppm for
307 different almandine garnets sampled from sediments. In summary, the amount of these two
308 elements can vary, but it appears that they typically show concentrations from tens to a couple of
309 several hundreds of ppm in most almandines. The amounts of Mn^{3+} are not known.

310 Many spessartines can be described well by the system spessartine-almandine with lesser
311 amounts of pyrope and grossular components (Deer et al. 1982), but more unusual compositions
312 have been documented. Some spessartines can show more chemical variability than almandine-
313 rich crystals. Less research has been done on measuring different minor and trace elements in
314 spessartine compared to almandine or pyrope. That said, there is a class of spessartine-pyrope
315 garnets that contain small amounts of V_2O_3 (0.09-0.68 wt. %) and Cr_2O_3 (0.04-0.63 wt. % - see
316 Manson and Stockton 1984 for these results but see also Schmetzer et al. 2001). These transition
317 metals can affect markedly the color of these crystals. There is also a class of seldom occurring
318 spessartine-andradite rich garnets (see Korinevsky 2015). The spessartine-almandine garnets
319 studied here (Table 1b) do not appear to have significant amounts of V_2O_3 and Cr_2O_3, so as to
320 give rise to absorption bands in the visible region. Any possible Fe_2O_3 in spessartine is not
321 thought to affect the results of this study. It may, though, play a role in affecting the nature of the
322 O → M CT edge (Taran et al. Part II and Geiger and Taran Part III) as could possibly TiO_2 as
323 well.

Based on current crystal chemical understanding of "lower pressure" aluminosilicate garnets and with regard to the behavior of transition metals cations, the triangular dodecahedrally coordinated X cation is Fe^{2+} and/or Mn^{2+}. Trivalent and tetravalent charged transition-metal cations are mostly (or exclusively) located at the octahedral site.

Spectral analysis

As discussed above, various electronic transitions can occur in crystals and silicate garnet is an interesting system for studying them. We focus our analysis in this investigation on the spin-forbidden transitions relating to Fe^{2+} and Mn^{2+}. Fe^{3+} is also considered as it can occur in small amounts in many garnets. Our approach is a first-order experimental one and empirical. We focus our attention on energy behavior of different electronic transitions as a function of garnet composition. Taran et al. (Part II) and Geiger and Taran (Part III) focus on the physical nature of different absorption features and their spectroscopic assignments.

Spectra of almandine-pyrope solid solutions

The early experimental investigations of Moore and White (1972) and White and Moore (1972) provide a good starting point in the study of Fe^{2+}, Mn^{2+} and Fe^{3+} electronic transitions in garnets of different composition. They measured the UV/Vis/NIR spectra of a number of silicate garnets, including various composition almandines, pyropes and spessartines and concentrated their investigation on the crystal field electronic absorption bands. Unfortunately, full spectra for many of their studied garnets are not shown. They labeled their observed electronic absorption transitions with increasing energy with the letters "a to c" for Fe^{2+} spin-allowed bands and "d to r" for the various Fe^{2+}, Mn^{2+} and Fe^{3+} spin-forbidden bands. The energies of the spin-forbidden bands "d" to "r" bands are given for all their samples in Moore and White (1972). Taran et al. (Part II) measured the spectra of an almandine and an almandine-bearing pyrope and analyzed further the different Fe^{2+} and Fe^{3+} transitions that can occur. A couple of absorption features that were not noted by Moore and White (1972) and/or possibly incorrectly assigned are discussed in

the former work and the results of the latter workers are partly modified. Taran et al. also give an up-to-date analysis on the assignments for the spin-forbidden bands of Fe^{2+}, Mn^{2+} and Fe^{3+}.

Energy behavior of spin-forbidden Fe^{2+} transitions. We measured the UV/Vis single-crystal spectra for a number of natural garnets belonging to the almandine-pyrope solid solution. The amounts of Ca and Mn^{2+} are, in general, low (Table 1a). Figure 2 shows a stacked plot of UV/Vis absorption spectra of eight representative garnets with different $Fe^{2+}/(Fe^{2+} + Mg)$ ratios. A number of spin-forbidden absorption bands can be observed. We consider those related to $^{VIII}Fe^{2+}$ first. Bands d to h are observed in most spectra and f, g and h are the most intense. Bands d, e, f and g are broader than the higher wavenumber bands. Band i is expressed as a weak high-energy shoulder on the intense band h. Band j* needs special comment. It is observed as a weak poorly defined absorption feature in some of the almandine-pyrope garnet spectra. Moore and White (1972) assigned it to a spin-forbidden band of Mn^{2+}. However, it can be observed in spectra of some garnets with no measurable Mn^{2+}. In addition, it can be obtained in spectral deconvolutions of almandine and pyrope-almandine garnets (Taran et al. Part II). This weak feature could, therefore, be related to a Fe^{2+} transition. Bands k and q appear to be weaker in intensity than bands d to g and are best observed in the spectra of almandine-rich garnets. A few almandine spectra (e.g., GRR 3256) appear to show a weak shoulder on the high-energy edge of band k. Finally, there appears to be a weak spectral feature occurring between band m and q at about 24200-24300 cm^{-1} (see Taran et al. Part II, for further discussion on modified and more complete band labels and assignments). Because we observe this weak feature in the spectra of garnets with no measurable Mn^{2+}, we think, once again, it is best assigned to Fe^{2+}.

Supplementary Table 2a lists the wavenumbers of various Fe^{2+} spin-forbidden bands, as based on an analysis of their peak maxima, as far as this is possible (e.g., energies for band i are estimates) for the different almandine-pyrope garnets studied herein (Table 1a). The results agree to first order with previously published values. The energy behavior of these bands is shown in

Figure 3 as a function of almandine content in the solid-solution crystals. Bands d, e, and f decrease slightly in energy, less than 125 cm^{-1}, with increasing pyrope component across the join. Bands h, i, and k, in contrast, increase slightly in energy between about 80 to 150 cm^{-1} with increasing pyrope component. The highest wavenumber band q increases the most in energy (~325 cm^{-1}) going from nearly end-member almandine to nearly end-member pyrope.

Energy behavior of spin-forbidden Fe^{3+} transitions. Moore and White (1972) assigned the three bands l, m and r to electronic transitions of Fe^{3+} located at the octahedral site of garnet. These bands can be observed in the spectra of many almandine-pyrope garnets, especially band r, which is the most intense of the three (Fig. 2). Their energy behavior as a function of almandine content is shown in Figure 3. All three bands appear to increase in energy from near-end-member almandine to near end-member pyrope especially bands m and r.

Spectra of almandine-spessartine solid solutions

The UV/Vis spectroscopic investigations of Moore and White (1972), Smith and Langer (1983), and Taran et al. (Part II) provide a starting point for the analysis of our spectra of almandine-spessartine solid-solutions (Table 1b). The amounts of Ca and Mg^{2+} are, in general, low, but a couple of crystals have more extended compositions and are best described as pyrope-almandine-spessartine garnets (e.g., GRR 83). Figure 4 shows a stacked plot of seven UV/Vis absorption spectra for garnets with different spessartine contents. The intent is to primarily document the behavior of the most narrow and intense Mn^{2+} spin-forbidden bands located between 23000 and 25000 cm^{-1}. We consider the energies of the Fe^{2+} electronic transitions first.

Energy of spin-forbidden Fe^{2+} transitions. Supplementary Table 2b lists the various Fe^{2+} absorption bands and their wavenumbers for the studied almandine-spessartine garnets. The wavenumbers are plotted as a function of almandine content in Figure 5. The lowest wavenumber

bands d, e and f increase in energy between 300 to 425 cm^{-1} with increasing spessartine component across the join. Bands g, h, i and k show less change in energy across the binary. The energies of bands h and k do not vary significantly, band g may decrease slightly and band i may increase with increasing spessartine in the garnet, but these variations may be within the level of experimental uncertainty. Band q, which is weak in intensity, was not recorded in many spectra and, therefore, is not considered.

Energy of spin-forbidden Mn^{2+} transitions. Supplementary Table 2b lists several Mn^{2+} absorption bands and their wavenumbers for a number of the studied almandine-spessartine garnets (Table 1b). Only the energies of the bands that could be determined with some degree of precision are listed and they are the four relatively intense narrow ones located between 23000 and 25000 cm^{-1}. Lower wavenumber Mn^{2+} bands (Taran et al. Part II) are weaker in intensity and broader and are, therefore, not considered. Figure 6 shows the energy behavior of these Mn^{2+} spin-forbidden bands as a function of spessartine component in the garnet. A simple first-order analysis indicates that bands n´ and p increase slightly in energy with increasing spessartine and decreasing almandine content in the solid solution. The opposite behavior is the case for bands n and o. However, we note that this result is a bit tentative, because of scatter in the data and/or incomplete data coverage for more spessartine-poor compositions.

Spin-forbidden Fe^{3+} transitions. The energies of the three bands l, m and r for several almandine-rich garnets are shown in Figure 5. Fe^{3+}-O bonding, based on the energies of these bands, is discussed below.

Crystal chemistry and Fe^{2+}-O and Mn^{2+}-O bond behavior of almandine-pyrope and almandine-spessartine solid solutions

There are many research reports on aluminosilicate garnet, $\{X^{2+}_3\}[Al_2](Si_3)O_{12}$, at the microscopic scale. For solid solutions, atomic exchange occurs at $\{X^{2+}\}$ and it causes variations in local structure properties within the crystal. X^{2+}-O chemical bonding should be affected. Structural relaxation occurs within the triangular dodecahedron sublattice, but neighboring octahedra (and tetrahedra) are affected as well because they share polyhedral edges with the former (Fig. 1). A crystal-chemical analysis of solid-solution behavior is simplified in garnet, compared to many other silicates, because it has a high symmetry (*Ia*-3*d*) and by the fact that all three cations are located on special crystallographic positions and the single crystallographic anion ligand (i.e., oxygen) is located at a general *x*, *y*, *z* position (Novak and Gibbs 1971; Armbruster et al. 1992; Merli et al. 1995). Thus, local structural relaxation is associated with the oxygen ions, as is macroscopic relaxation for the crystal as a whole.

Experimental study has been made on how the two crystallographically independent X^{2+}-O bond lengths behave in binary solid solutions using X-ray absorption (Fe and Mn) fine structure spectroscopy (Sani et al. 2004) and NIR absorption spectroscopy of spin-allowed Fe^{2+} bands (Geiger and Rossman 1994) as well by single-crystal diffraction methods (Armbruster et al. 1992). Bond behavior and local structural variations in garnet solid solutions have also been investigated computationally (e.g., Bosenick et al. 2000; Geiger et al. 2003; Freeman et al. 2006).

Sani et al. (2004) measured the Fe^{2+}-O and Mn^{2+}-O bond lengths for several synthetic almandine-spessartine garnets. The spectra indicated that the two different Fe^{2+}-O bonds did not vary in length, that is Fe(1)-O (or alternatively the label Fe-O(2)) were ~2.21 Å and Fe(2)-O (or Fe-O(4)) bonds were ~2.35 Å across the binary. In contrast, the shorter Mn(1)-O (or Mn-O(2)) bond remained constant in length with a value of ~2.24 Å, whereas the longer Mn(2)-O bond (or Mn-O(4)) increased slightly in length from about 2.37 Å to about 2.43 Å going from almandine-rich to more spessartine-rich garnet compositions. Geiger and Rossman (1994) investigated Fe^{2+}-O bond behavior for the almandine-pyrope and almandine-spessartine binaries by measuring the three highest energy spin-allowed absorption bands of Fe^{2+} occurring in the NIR region. They

454 originate from the split $^5E_g \rightarrow {}^5T_{2g}$ electronic transition for symmetry descending from O_h (cubic)
455 to D_2 (dodecahedral) (e.g. White and Moore 1972 - It should be noted that this latter type of
456 spectroscopy is more sensitive to variations in bond length than the former, but numerical values
457 cannot be obtained). It was argued that Fe^{2+}-O bond length (note that the two crystallographically
458 independent Fe^{2+}-O bonds could not be measured spectroscopically and that the analysis only
459 considers a single undifferentiated Fe^{2+}-O bond) decreases slightly in length with increasing
460 pyrope component in the garnet. This is expected because pyrope has a smaller molar volume
461 (i.e., 11.3157(16) J/bar, where the radius of Mg^{2+} = 0.89 Å - Geiger and Feenstra 1997 and
462 Shannon 1976) than almandine (i.e., 11.523(6) J/bar, where the radius of Fe^{2+} = 0.92 Å). In other
463 words, a model of Pauling limit behavior (or the state of alternation bonds) involving slight Fe^{2+}-
464 O bond shortening describes the behavior across the join (see Geiger 2008). The behavior of
465 Fe^{2+}-O bonds in almandine-spessartine solid solutions was more difficult to interpret. Here,
466 assuming Pauling limit behavior is operating, it could be expected that Fe^{2+}-O bonds should
467 increase slightly in length with increasing spessartine in the garnet. This is because the molar
468 volume of spessartine (i.e., 11.796(3) J/bar, where the radius of Mn^{2+} = 0.96 Å - Geiger and
469 Feenstra 1997 and Shannon 1976) is greater than that of almandine. However, the general
470 increase in energy of at least two of the three Fe^{2+} T_{2g} bands with increasing spessartine in the
471 garnet does not appear to support the assumed model behavior.
472 Consider now the present UV/Vis spectroscopic results and the energy behavior of the
473 different Fe^{2+} spin-forbidden transitions in almandine-pyrope garnets. An analysis of the
474 transition energies indicates that variations as a function of garnet composition occur. Those of
475 the lower wavenumber bands d, e, and f appear to decrease slightly between roughly 90 to 125
476 cm^{-1} starting from nearly end-member almandine to nearly end-member pyrope (Fig. 3). The
477 energy of the transition given by band g does not vary as a function of garnet composition. In
478 contrast, bands h, i, and k appear to increase in energy (between 80 and 150 cm^{-1}) with increasing

pyrope component in the garnet. Finally, the highest wavenumber transition, given by band q, increases the most by about 325 cm^{-1} across the join.

These bands represent different spin-forbidden electronic transitions among the five split Fe^{2+} *d* orbitals occurring in the triangular dodecahedral crystal field. White and Moore (1972) analyzed geometrically the *d* orbital placement within a cube (i.e., the triangular dodecahedron in garnet can be described as a distorted cube) with respect to the relative energies of the different spin-allowed Fe^{2+} transitions. Geiger and Rossman (1994) and Geiger et al. (2003) modified their analysis taking into account a more recent and currently accepted transition scheme of Newman et al (1978). Following this, the d_{z^2} and d_{xy} orbitals should have the least electronic repulsion with O^{2-} ligands located at the cube corners, because the lobes of both orbitals point to the centers of cube faces. The d_{z^2} orbital is taken as the ground state and d_{xy} the next highest energy for the two lowest energy E_g split states of Fe^{2+}. For the three higher energy T_{2g} split levels, the d_{yz} orbital energy should be the most stable and d_{xz} the least due to the D_2 geometry of the triangular dodecahedron. The orbital $d_{x^2-y^2}$ should be intermediate in energy between these two states. Following this and assuming, once again, a model of Pauling limit behavior involving slight local Fe^{2+}-O bond compression with increasing pyrope in a garnet crystal, it can be argued that those spin-forbidden Fe^{2+} bands showing the greatest changes in energy with varying garnet composition should involve transitions between the d_{yz}, $d_{x^2-y^2}$ and d_{xz} orbitals. In other words, these orbitals should be the most sensitive to local positional relaxation of the single O^{2-} ligand in *x*, *y* and *z*. The Fe^{2+} electronic transition given by highest wavenumber band q could involve d_{xz}, because it should have the largest repulsion with the *p* orbitals of O^{2-}. Those transitions that decrease slightly in energy with increasing pyrope component in the garnet (i.e., the lowest wavenumber bands d, e and f) would involve local oxygen shifts in *x*, *y* and *z* that decrease the degree of iron orbital-oxygen orbital repulsion. The spectroscopic and diffraction results give a fairly consistent crystal-chemical picture of solid-solution behavior for almandine-pyrope garnets.

505 It is more difficult to construct a consistent crystal-chemical and bonding model for
506 almandine-spessartine garnets, as based on the existing data. Here, the energy behavior of Fe^{2+}
507 spin-allowed bands (Geiger and Rossman 1994) does not support a crystal-chemical model with
508 Pauling limit behavior, whereby local Fe^{2+}-O bonds increase in length with increasing spessartine
509 in the garnet. What is the Fe^{2+} spin-forbidden transition energy behavior for this solid solution
510 and can it be explained? For this garnet system, the lowest wavenumber bands d, e and f appear
511 to vary the most in energy (i.e., between roughly 300 and 400 cm^{-1}) compared to those of the
512 higher wavenumber transitions given by bands g, h, i and k (i.e., < 100 cm^{-1}). All transitions
513 increase in energy with increasing spessartine in the garnet (Fig. 5). This is different than the
514 general energy behavior exhibited by Fe^{2+} electronic transitions in almandine-pyrope garnets,
515 where energies can decrease or increase across the join.
516 The energy behavior of four higher wavenumber spin-forbidden Mn^{2+} transitions (bands
517 n′, n, o and p) across the almandine-spessartine binary is shown in Figure 6. Mn^{2+} has different
518 electronic behavior compared to Fe^{2+} because of the former's d^5 electronic configuration.
519 Chemical bonding should also be different. Should the energy trends laid out by the data be
520 correct, the behaviors of the four different Mn^{2+} electronic transitions of relatively similar
521 wavenumbers are dissimilar. It is difficult to interpret the spectroscopic results more fully
522 because assignments for all the Mn^{2+} electronic transitions have not been successful. A
523 satisfactory analysis of spessartine's UV/Vis spectrum, based on crystal field theory and the use
524 of Tanabe-Sugano diagrams with O_h symmetry, cannot be obtained (Taran et al. Part II).
525 We conclude that the NIR and Vis/Uv spectroscopic results on spin-allowed and spin-
526 forbidden Fe^{2+} electronic transitions, respectively, indicate that the transition energy behavior of
527 this cation and its bonding with oxygen are different in almandine-pyrope and almandine-
528 spessartine garnets. Obtaining a better understanding of electronic transition energy behavior is
529 complex for a couple of reasons and further research is needed. The vibrational behavior of Fe^{2+}
530 in almandine is anisotropic in nature, as shown by X-ray diffraction and ^{57}Fe Mössbauer

spectroscopic measurements on synthetic end-member almandine (Armbruster et al. 1992; Geiger et al. 1992) and a natural almandine solid-solution crystal (Bull et al. 2012). The interatomic potential involving Fe^{2+} is probably fairly anharmonic as well (see Geiger 2013). It is not known how vibrational anisotropy and anharmonicity vary in almandine-bearing solid solutions and how they can affect local electronic-transition and chemical-bonding properties. Computational studies on pyrope-grossular, $\{Mg_{3x},Ca_{3-3x}\}[Al_2](Si_3)O_{12}$, solid solutions (Bosenick et al. 2000; Freeman et al. 2006) show that the longer X-O(4) bonds for both Mg and Ca vary more in length compared to shorter X-O(2) bonds across this garnet binary. Such calculations are needed on almandine-bearing garnet solid solutions.

It may be noted, in concluding and in a related sense, that ^{57}Fe Mössbauer measurements on almandine-containing binary solid solutions do not show significant variations in their hyperfine parameters (Geiger et al. 2003). Specifically, the isomer shift, which is a measure of the *s* electron contact density at the Fe^{2+} nucleus, and which is affected by the nature of and screening by the *d* bonding orbitals, is not measurably different between $\{Mg_{3x}Fe^{2+}_{3-3x}\}$-$[Al_2](Si_3)O_{12}$ and $\{Mn^{2+}_{3x}Fe^{2+}_{3-3x}\}[Al_2](Si_3)O_{12}$ garnets (i.e., 1.27 ± 0.01 mm/sec at RT and 1.41 ± 0.01 at 77 K - Geiger et al. 2003). The explanation for this observation is that the Fe^{2+}-O bonds are highly ionic (Lyubutin and Dodokin 1971; Evans and Sergent 1975; Geiger et al. op. cit.) and any covalent contributions, regardless of the garnet composition, are not reflected in the hyperfine parameters.

Fe^{3+} and Fe^{3+}-O bonding in aluminosilicate garnet

The study of Moore and White (1972) shows that Fe^{3+} can be present in almandine, as based on their interpretation of the spin-forbidden Fe^{3+} bands l, m and r. Later works, both experimental (Smith and Langer 1983) and theoretical (Guo-Yin and Min-Guang 1984) challenged the assignments for these three bands especially for the most intense band r. We accept Moore and White's interpretation (see Taran et al. Part II, for a detailed discussion of

these bands and their intensity behavior). Following this and based on the spectra of this work, it appears that many, if not nearly all, almandine-pyrope garnets contain some Fe^{3+}. This is a notable result.

In terms of crystal chemistry, an analysis of Fe^{3+}-O^{2-} bonding behavior is possible using the measured UV/Vis spectra and published results. A measure of the covalent bonding between a central ion and its surrounding ligands can be described by the Racah *B* parameter (see discussion in Burns 1993). The other Racah parameter is *C*. The relevant equations are:

$$^6A_{1g} \rightarrow {}^4A_{1g}, {}^4E_g\,(^4G)\text{: } \nu_3 = 10B + 5C \quad (2),$$

and

$$^6A_{1g} \rightarrow {}^4E_g\,(^4D)\text{: } \nu_5 = 17B + 5C \quad (3),$$

from which one obtains

$$\nu_5 - \nu_3 = 7B \quad (4).$$

The energies of bands l and m and the energy of band r come into play. Consider garnet GTF 90-28 with about 71 mol % almandine, for example (Table 1a). Taking ν_3 as the mean value of the energies of the l and m bands, one obtains $B \approx 557$ and $C \approx 3522$ cm^{-1}. For the case of $^{VI}Fe^{3+}$ in grossular, one has 714 and 2972 cm^{-1} using the spectral data in Moore and White (1972 - note that their published values of 614 and 3332 cm^{-1} appear to be incorrect), and for $^{VI}Fe^{3+}$ in andradite 613 and 3308 cm^{-1} (Platonov and Taran 2018). Because the *B* parameter is lowest for almandine, its Fe^{3+}-O^{2-} bond is slightly more covalent compared to Fe^{3+}-O^{2-} bonds in the Ca-rich garnets grossular and andradite. The Fe^{3+}-O^{2-} bond length in end-member andradite is 2.0201(5) Å (Armbruster and Geiger 1993) and the Al^{3+}-O^{2-} bond length is 1.8904(4) Å in end-member almandine (Armbruster et al. 1992). Thus, it should be expected that a local Fe^{3+}-O^{2-} bond in almandine could be very slightly shorter than in andradite. Band r in the spectrum of andradite occurs at lower energy (i.e., 26800 cm^{-1}) than in almandine (i.e., ~27050 cm^{-1}).

The Fe^{3+} bands l & m and r vary in energy more as a function of bulk garnet composition than Fe^{2+}-related bands (Fig. 3). The shorter Fe^{3+}-O chemical bonds should be more covalent than

This is the peer-reviewed, final accepted version for American Mineralogist, published by the Mineralogical Society of America.
The published version is subject to change. Cite as Authors (Year) Title. American Mineralogist, in press.
DOI: https://doi.org/10.2138/am-2022-8499. http://www.minsocam.org/

583 the longer Fe^{2+}-O bonds and the electronic state of Fe^{3+} is apparently more affected by its crystal-
584 chemical surroundings than Fe^{2+} (Fig. 1b and d). The longer Fe^{2+}-O bonds should be highly ionic
585 in nature and the electronic state of Fe^{2+} is affected little by changes in its immediate ligand
586 surroundings.
587
588 **IMPLICATIONS**
589 The microscopic properties and crystal-chemical behavior of various silicate garnet solid-
590 solution systems are slowly being revealed with time. Further study of a more quantitative nature,
591 compared to what has been done in the past, is now needed.
592 From an experimental standpoint, several areas of research could be done. First, work is
593 required to better standardize spectra. There is no consensus on how to report UV/Vis band
594 energies and their uncertainties. Large numbers of spectra on garnet have been recorded over
595 many years using many different experimental set-ups, but it is difficult to compare and analyze
596 reported band energies. Standards, as used in most types of experimental measurements, are
597 required. Second, further spectroscopic measurements on other solid-solution aluminosilicate
598 garnets are needed. This is necessary in order to obtain a broader and more systematic description
599 of Fe^{2+} and Mn^{2+} electronic and chemical-bonding behavior. Variations in local properties and
600 structural heterogeneity in almandine-pyrope-spessartine garnets can be expected to be
601 considerably greater with the incorporation of the large Ca^{2+} cation when it replaces Fe^{2+} Mg, and
602 Mn^{2+}. It remains to be determined how Fe^{2+} and Mn^{2+} electronic transitions, spin allowed for Fe^{2+}
603 and spin forbidden for both cations, will be affected. Third, the nature of band broadening for
604 spin-forbidden and spin-allowed transitions in intermediate composition garnets has not been
605 explored. Both could possibly carry some information on local structural heterogeneity through
606 their band widths. As best we know, there has been little, if any, research made in this direction at
607 least in terms of minerals. Fourth, more study relating to Fe^{3+} contents in aluminosilicate garnets,
608 using UV/Vis spectra obtained with a microscope, could prove interesting. Determining small

609 Fe^{3+} contents from microprobe analyses and assuming stochiometric considerations are fraught
610 with uncertainty. ^{57}Fe Mössbauer measurements are typically made using powders and, thus,
611 zoning determinations in crystals cannot be undertaken. Moreover, the method is not precise at
612 small Fe^{3+} concentrations. X-ray absorption studies (XANES) on Fe^{3+} amounts require access to a
613 synchrotron and the interpretation and fitting of spectra are not necessarily straightforward.
614 Finally, there exists little work on interpreting the spectra of complex silicates using
615 advanced bonding theories and state-of-the-art electronic structure calculations. Studies
616 combining quantitative spectroscopic measurements with simulations will yield a deeper physical
617 understanding of electronic transition and bonding behavior. In terms of garnet solid solutions,
618 local structural relaxation behavior and how it affects bonding needs study. Many experimental
619 results alone are either too blunt or are difficult to quantify for such subtle structural variations.
620 To begin, electronic structure calculations on end-member spessartine and almandine should be
621 possible. Studying garnet solid-solution systems will be a greater challenge.
622

623 **ACKNOWLEDGMENTS**

624 Several different individuals and sources provided garnet samples used in this study. In the cases
625 where they are known, they are listed in Tables 1a and 1b. We thank the various institutions and
626 individuals for their generosity. We also thank O. A. Vyshnevskyi (Kiev) for making microprobe
627 EDS analyses on the samples studied spectroscopically in Kiev and M. Grodzicki (Salzburg) for
628 helpful discussions on crystal/ligand field theory. U. Hålenius and an anonymous referee are
629 thanked for their useful comments that improved the manuscript. This research was supported by
630 a grant to C.A.G. from the Austrian Science Fund (FWF: P 30977-NBL). He also thanks the
631 "Land Salzburg" for financial support through the initiative "Wissenschafts- und
632 Innovationsstrategie Salzburg 2025".
633
634

635 **REFERENCES CITED**

636

637 Armbruster, T., and Geiger, C.A. (1993) Andradite crystal chemistry, dynamic X-site disorder
638 and strain in silicate garnets. European Journal of Mineralogy, 5, 59-71.
639 Armbruster, T., Geiger, C.A., and Lager, G.A. (1992) Single crystal X-ray refinement of
640 almandine pyrope garnets at 298 and 100 K. American Mineralogist, 77, 512-523.
641 Aparicio, C., Filip, J., Skogby, H., Marusak, Z., Mashlan, M., and Zboril, R. (2012) Thermal
642 behavior of almandine at temperatures of 1,200°C in hydrogen. Physics and Chemistry of
643 Minerals, 39, 311-318.
644 Boeke, H.E. (1914) Die Granatgruppe. Eine statistische Untersuchung. Zeitschrift für
645 Kristallographie, 53, 149-157.
646 Boiocchi, M., Bellatreccia, F., Della Ventura, G., and Oberti, R. (2012) On the symmetry and
647 atomic ordering in (OH,F)-rich spessartine: towards a new hydrogarnet end-member.
648 Zeitschrift für Kristallographie, 227, 385-395.
649 Bosenick, A., Dove, M.T., and Geiger, C.A. (2000) Simulation studies of pyrope-grossular solid
650 solutions. Physics and Chemistry of Minerals, 27, 398-418.
651 Bressler, C.T. (1945/1946) Garnet deposits near Wrangell southeastern Alaska. Geological
652 Survey Bulletin, 963-C, 81-93.
653 Bull, J.N., Tennant, W.C., Boffa Ballaran, T., Nestola, F. and McCammon, C.A. (2012)
654 Anisotropic mean-squared-displacement tensor in cubic almandine garnet: a single crystal
655 ^{57}Fe Mössbauer study. Physics and Chemistry of Minerals, 39, 561-575.
656 Burns, R.G. (1970; 1993) Mineralogical Applications of Crystal Field Theory. First (1970) and
657 Second (1993) editions. Cambridge University Press, Cambridge, England. 551 p (2nd
658 Edition).
659 Clark, S.P., Jr. (1957) Absorption spectra of some silicates in the visible and near infrared.
660 American Mineralogist, 42, 732-742.

661 Copjaková, R., Sulovský, P. and Paterson, B. (2005) Major and trace elements in pyrope-
662 almandine garnets as sediment provenance indicators of the Lower Carboniferous Culm
663 sediments, Drahany Uplands, Bohemia Massif. Lithos, 82, 51-70.
664 Dachs, E., Geiger, C.A., and Benisek, A. (2012) Almandine: Lattice and non-lattice heat capacity
665 behavior and standard thermodynamic properties. American Mineralogist, 97, 1771-1782.
666 Deer, W.A., Howie, R.A. and Zussman, J. (1982) Orthosilicates. Volume 1A, Second Edition.
667 Longman House, Burnt Hill, U.K. 919 p.
668 Evans, B.J. and Sergent, E.W., Jr. (1975) ^{57}Fe NGR of Fe phases in “magnetic cassiterites”.
669 Contributions to Mineralogy and Petrology, 53, 183-194.
670 Freeman, C.L., Allan, N.L, and van Westrenen, W. (2006) Local cation environments in the
671 pyrope-grossular $Mg_3Al_2Si_3O_{12}$-$Ca_3Al_2Si_3O_{12}$ garnet solid solution. Physical Review,
672 B74, 134203-1-134203-9.
673 Geiger, C.A. (2004) Spectroscopic investigations relating to the structural, crystal-chemical and
674 lattice-dynamic properties of $(Fe^{2+},Mn^{2+},Mg,Ca)_3Al_2Si_3O_{12}$ garnet: A review and analysis.
675 In European Notes in Mineralogy - Spectroscopic Methods in Mineralogy, E. Libowitzky
676 & A. Beran, Eds., v. 6, 589-645.
677 Geiger, C.A. (2008) Silicate garnet: A micro to macroscopic (re)view. American Mineralogist,
678 93, 360-372.
679 Geiger, C.A. (2013) Static disorders of atoms and experimental determination of Debye
680 temperature in pyrope: Low- and high-temperature single-crystal X-ray diffraction study -
681 - Discussion. American Mineralogist, 98, 780-782.
682 Geiger, C.A. (2016) A tale of two garnets: The role of solid solution in the development toward a
683 modern mineralogy. American Mineralogist, 101, 1735-1749.
684 Geiger, C.A. and Feenstra, A. (1997) Molar volumes of mixing of almandine-pyrope and
685 almandine-spessartine garnets and the crystal chemistry of aluminosilicate garnets.
686 American Mineralogist, 82, 571-581.

687 Geiger, C.A. and Rossman, G.R. (1994) Crystal field stabilization energies of almandine-pyrope
688 and almandine-spessartine garnets determined by FTIR near infrared measurements.
689 Physics and Chemistry of Minerals, 21, 516-525.
690 Geiger, C.A. and Rossman, G.R. (2018) IR spectroscopy and OH^- in silicate garnet: The long
691 quest to document the hydrogarnet substitution. American Mineralogist, 103, 384-393.
692 Geiger, C.A. and Taran, M.N. (submitted) UV/Vis single-crystal absorption spectroscopy of
693 garnet: Part III. $^{VIII}Fe^{2+} + {}^{VI}Fe^{3+} \rightarrow {}^{VIII}Fe^{3+} + {}^{VI}Fe^{2+}$ charge transfer in aluminosilicate
694 garnets. American Mineralogist.
695 Geiger, C.A., Langer, K., Bell, D.R., Rossman, G.R. and Winkler, B. (1991) The hydroxide
696 component in synthetic pyrope. American Mineralogist, 76, 49-59.
697 Geiger, C.A., Armbruster, T., Lager, G.A., Jiang, K., Lottermoser, W., and Amthauer, G. (1992)
698 A combined temperature dependent Mössbauer and single crystal X-ray diffraction study
699 of synthetic almandine: Evidence for the Gol`danskii-Karyagin effect. Physics and
700 Chemistry of Minerals, 19, 121-126.
701 Geiger, C.A., Stahl, A., and Rossman, G.R. (2000) Single-crystal IR- and UV/VIS-spectroscopic
702 measurements on transition-metal-bearing pyrope: The incorporation of hydroxide in
703 garnet. European Journal of Mineralogy, 12, 259-271.
704 Geiger, C.A., Grodzicki, M., and Amthauer, G. (2003) The crystal chemistry and Fe^{II} site
705 properties of aluminosilicate garnet solid solutions as revealed by Mössbauer
706 spectroscopy and electronic structure calculations. Physics and Chemistry of Minerals, 30,
707 280-292.
708 Guo-Yin, S. and Min-Guang, Z. (1984) Analysis of the spectrum of Fe^{2+} in Fe-pyrope garnets.
709 Physical Review B, 30, 3691-3703.
710 Hickmott, D.D., Shimizu, N., Spear, F.S., and Selverstone, J. (1987) Trace-element zoning in a
711 metamorphic garnet. Geology, 15, 573-576.

712 Khomenko, V.M., Langer, K., Wirth, R., and Weyer, B. (2002) Mie scattering and charge
713 transfer phenomena as causes of the UV edge in the absorption spectra of natural and
714 synthetic almandine garnets. Physics and Chemistry of Minerals, 29, 201-209.
715 Korinevsky, V.G. (2015) Spessartine-andradite in scapolite pegmatite, Ilmeny Mountains, Russia.
716 The Canadian Mineralogist, 53, 623-632.
717 Krambrock, K., Guimarães, F.S., Pinheiro, M.V.B., Paniago, R., Righi, A., Persiano, A.I.C.,
718 Karfunkel, J., and Hoover, D.B. (2013) Purplish-red almandine garnets with alexandrite-
719 like effect: causes of colors and color-enhancing treatments. Physics and Chemistry of
720 Minerals, 40, 555-562.
721 Lyubutin, I.S. and Dodokin, A.P. (1971) Temperature dependence of the Mössbauer effect for
722 Fe^{2+} in dodecahedral coordination in garnet. Soviet Physics-Crystallography, 15, 1091-
723 1092.
724 Manning, P.G. (1967) The optical absorption spectra of the garnets almandine-pyrope, pyrope,
725 and spessartine and some structural interpretations of mineralogical significance.
726 Canadian Mineralogist, 9, 237-251.
727 Manning, P.G. (1972) Optical absorption spectra of Fe^{3+} in octahedral and tetrahedral sites in
728 natural garnets. Canadian Mineralogist, 11, 826-839.
729 Manson, D.V. and Stockton, C.M. (1984) Pyrope-spessartine garnets with unusual color
730 behavior. Gems and Gemology, Winter, 200-207.
731 Marfunin, A.S. (1979) Physics of mineral and inorganic materials. Springer. Berlin. 340 p.
732 Merli, M., Callegari, A., Cannillo, E., Caucia, F., Leona, M., Oberti, R., and Ungaretti, L. (1995)
733 Crystal-chemical complexity in natural garnets: structural constraints on chemical
734 variability. European Journal of Mineralogy, 7, 1239-1249.
735 Moore, R.K. and White, W.B. (1972) Electronic spectra of transition metal ions in silicate
736 garnets. Canadian Mineralogist, 11, 791–811.

737 Newman, D.J., Price, D.D. and Runciman, W.A. (1978) Superposition model analysis of the near
738 infrared spectrum of Fe^{2+} in pyrope-almandine garnets. American Mineralogist, 63, 1278-
739 1281.
740 Novak, G.A. and Gibbs, G.V. (1971) The crystal chemistry of the silicate garnets. American
741 Mineralogist, 56, 791-825.
742 Pabst, A. (1943) Large and small garnets from Fort Wrangell, Alaska. American Mineralogist,
743 28, 233-245.
744 Pinet, M. and Smith, D.C. (1994) Raman microspectrometry of garnets $X_3Y_2Z_3O_{12}$: II. The
745 natural aluminium series pyrope-almandine-spessartine. Schweizerische Mineralogische
746 und Petrographische Mitteilungen, 74, 161-179.
747 Platonov, A.N. and Taran, M.N. (2018) Optical spectra and color of natural garnets. Naukova
748 dumka, Kiev (in Russian). 255 p.
749 Rager, H., Geiger, C.A. and Stahl, A. (2003) Ti(III) in pyrope: A single-crystal electron
750 paramagnetic resonance study. European Journal of Mineralogy, 15, 697-699.
751 Runciman, W.A. and Marshall, M. (1975) The magnetic circular dichroism of pyrope-almandine
752 garnets. American Mineralogist, 60, 1122-1124.
753 Runciman, W.A. and Sengupta, D. (1974) The spectrum of Fe^{2+} ions in silicate garnets.
754 American Mineralogist, 59, 563-566.
755 Sani, A., Quartieri, S., Boscherini, F., Antonioli, G., Feenstra, A., and Geiger, C.A. (2004)
756 Atomistic-scale structural and dynamic properties of almandine-spessartine solid
757 solutions: An XAFS study at the Fe and Mn K-edges. European Journal of Mineralogy,
758 16, 801-808.
759 Schmetzer, K., Hainschwang, T., Kiefert, L., and Bernhardt, H-J. (2001) Pink to pinkish orange
760 malaya garnets from Bekily, Madagascar. Gems and Gemology, Winter, 296-302.
761 Schwandt, C.S., Papike, J.J, and Schearer, C.K. (1996) Trace element zoning in pelitic garnet of
762 the Black Hills, South Dakota. American Mineralogist, 81, 1195-1207.

763 Shannon, R.D. (1976) Revised effective ionic radii and systematic studies of interatomic
764 distances in halides and chalcogenides. Acta Crystallographica, A32, 751-767.
765 Slack, G.A. and Chrenko, R.M. (1971) Optical absorption of natural garnets from 1000 to 30000
766 wavenumbers. Journal of Optical Society of America, 61, 1325-1329.
767 Smith, G. and Langer, K. (1983) High pressure spectra up to 120 kbars of the synthetic garnet
768 end members spessartine and almandine. Neues Jahrbuch für Mineralogie - Monatshefte,
769 12, 541-555.
770 Sobolev, N.V. (1964) Classification of rock-forming garnets. Doklady Akademii Nauk SSSR,
771 157, 353-356.
772 Swanson, S.E. and Veal, W.B. (2010) Mineralogy and petrogenesis of pegmatites in the
773 Spruce Pine District, North Carolina, USA. Journal of Geosciences, 55, 27-42.
774 Taran, M.N, Langer, K. and Geiger, C.A. (2002) Single-crystal electronic absorption
775 spectroscopy on chromium, cobalt and vanadium-bearing synthetic pyropes at different
776 temperatures and pressures. Physics and Chemistry of Minerals, 29, 362-368.
777 Taran, M.N., Dyar, M.D. and Matsuyk, S.S. (2007) Optical absorption study of natural garnets of
778 almandine-skiagite composition showing intervalence $Fe^{2+} + Fe^{3+} \rightarrow Fe^{3+} + Fe^{2+}$ charge-
779 transfer transition. American Mineralogist, 92, 753-760.
780 Taran, M.N., Geiger, C.A., Vyshnevskyi, O.A. and Rossman, G.R. (submitted) Single-crystal
781 UV/Vis optical absorption spectra of almandine-bearing and spessartine Garnet: Part II.
782 An analysis of the spin-forbidden bands of Fe^{2+}, Mn^{2+}, and Fe^{3+}. American Mineralogist.
783 Taran, M.N. and Geiger, C.A. (in prep.) “Little ember of coal”: Part V. The color of almandine
784 and intermediate composition almandine-spessartine-pyrope garnets. American
785 Mineralogist.
786 White W.B. and Moore R.K. (1972) Interpretation of the spin-allowed bands of Fe^{2+} in silicate
787 garnets. American Mineralogist, 57, 1692-1710.

788 Woodland, A.B., Droop, G. and O'Neill, H.St.C. (1995) Almandine-rich garnet from near
789 Collobrieres, southern France, and its petrological significance. European Journal of
790 Mineralogy, 7, 187-194.
791 Zhou, K-W. and Zhao, S-B. (1984) The spin-forbidden spectrum of Fe^{2+} in silicate garnets.
792 Journal of Physics C: Solid State Physics, 17, 4625-4632.

This is the peer-reviewed, final accepted version for American Mineralogist, published by the Mineralogical Society of America.
The published version is subject to change. Cite as Authors (Year) Title. American Mineralogist, in press.
DOI: https://doi.org/10.2138/am-2022-8499. http://www.minsocam.org/

793 Table 1a. List and description of various natural and synthetic almandine-pyrope garnets (only those samples listed in Table 2a were considered in
794 the analysis of this work).

Garnet Species & Sample Label	Locality/ Synthesis Conditions	Sample Description	Composition
Synthetic Almandine A-2	$P(H_2O)$ = 15 kbar, T = 800 °C in iron capsule 24 hrs.	0.5-1 mm xtals, dark pink to red; Geiger & Rossman (1994); Geiger et al. (in prep.)	$Fe_{3.00}[Al_{1.91}Fe^{3+}_{0.09}]Si_{3.00}O_{12}$
Almandine FR-3	near Collobrières, France	0.24 mm, Metamorphosed ironstone; Woodland et al. (1995); Dachs et al. (2012)	$(Fe_{2.83}Mg_{0.07}Ca_{0.09})[Al_{1.92}Fe^{3+}_{0.08}]Si_{2.99}O_{12}$
Almandine A-5	near Collobrières, France	0.216 mm, MNHN 6956 (V); Pinet & Smith (1994); Geiger & Rossman (1994)	$(Fe_{2.82}Mg_{0.03}Mn_{0.04}Ca_{0.16})[Al_{2.05}Ti^{4+}_{0.01}]Si_{2.96}O_{12}$
Almandine JF-1	Zlaty Chlum near Jesenik, Czech Republic	0.50 mm, Aparicio et al. (2012); Geiger & Rossman (2018)	$(Fe_{2.85}Mg_{0.11}Mn_{0.02}Ca_{0.05})Al_{1.99}Si_{2.99}O_{12}$
Almandine GRR 3276	India (?)	0.213 mm, Faceted dark purplish red gem; unknown jewelry dealer	$(Fe_{2.5}Mg_{0.3}Mn_{0.1}Ca_{0.1})Al_{2.0}Si_{3.0}O_{12}$
Almandine A-12	Velusina, Macedonia, Yugoslavia	MNHN (V); Pinet & Smith (1994); Geiger & Rossman (1994)	$(Fe_{2.36}Mg_{0.50}Mn_{0.03}Ca_{0.07})Al_{2.10}Si_{2.95}O_{12}$
Almandine A-13	Portugal	0.71 mm, MNHN (V); Pinet & Smith (1994); Geiger & Rossman (1994)	$(Fe_{2.40}Mg_{0.26}Mn_{0.24}Ca_{0.06})Al_{2.07}Si_{2.96}O_{12}$
Almandine Jai-1	Jaipur, India	1.44 mm, Geiger & Rossman (1994)	$(Fe_{2.29}Mg_{0.73}Mn_{0.02}Ca_{0.03})Al_{2.01}Si_{2.96}O_{12}$
Almandine GRR 1040	North River, NY, USA	1.54 mm, deep reddish-purple slab; W.C. Oke collection Geiger & Rossman (1994)	$(Fe_{1.35}Mg_{1.30}Mn_{0.03}Ca_{0.26})Al_{1.99}Si_{3.01}O_{12}$
Almandine GRR 1056	Wrangell, AK, USA	1.10 mm; reddish-purple slab; Caltech reference	$(Fe_{2.03}Mg_{0.67}Ca_{0.18}Mn_{0.07})Al_{2.00}Si_{3.00}O_{12}$

		collection Pabst (1943); Bressler (1945/1946); Geiger & Rossman (1994)	
Almandine Lind 3	Rajasthan, India	1.06 mm, H. Lind	$(Fe_{2.05}Mg_{0.91}Ca_{0.03})[Al_{2.00}Fe^{3+}_{0.02}Ti_{0.01}]Si_{2.99}O_{12}$
Almandine GTF 90-28	Wrangell, AK, USA	0.56 mm, Pabst (1943); Bressler (1945/1946)	$(Fe_{2.13}Mg_{0.66}Ca_{0.14}Mn_{0.05})Al_{1.94}Si_{3.00}O_{12}$
Pyrope GRR 750	Zircon Point, Casey Bay, Enderby Land, Antarctica	E. Grew; Geiger & Rossman (1994)	$(Fe_{1.71}Mg_{1.25}Ca_{0.09}Mn_{0.02})Al_{2.04}Si_{2.97}O_{12}$
Pyrope GTF 90-33	De Luca pit, Emery Hill, Cortlandt, NY, USA	0.30 mm, orange-pink; hornfels; Taran et al. (2007)	$(Mg_{1.33}Fe_{1.29}Ca_{0.20}Mn_{0.06})[Al_{1.96}Fe^{3+}_{0.10}]Si_{2.99}Al_{0.01}O_{12}$
Pyrope SM 1597	Cowee Valley, North Carolina, USA	0.55 mm, rhodolite; A. Hofmeister; Taran et al. (2007)	$(Fe_{1.18}Mg_{1.70}Ca_{0.07}Mn_{0.04})[Al_{1.97}Ti_{0.01}]Si_{3.01}O_{12}$
Pyrope 200924473845	Africa	0.94 mm, 2.15 carat cut crystal, eBay, labeled "Almandine"	$(Fe_{1.18}Mg_{1.56}Ca_{0.25}Mn_{0.01})[Al_{1.92}Fe^{3+}_{0.08}]Si_{2.99}O_{12}$
Pyrope 200924659028	Africa	1.40 mm, cut crystal, eBay, labeled "Almandine"	$(Fe_{1.16}Mg_{1.45}Ca_{0.34}Mn_{0.05})[Al_{1.97}Fe^{3+}_{0.03}]Si_{2.99}O_{12}$
Pyrope 200939608981	Africa	0.97 mm, dark red, cut crystal, eBay, labeled "Almandine"	$(Fe_{1.18}Mg_{1.47}Ca_{0.31}Mn_{0.04})[Al_{2.00}]Si_{3.00}O_{12}$
Pyrope 17405755	Rakwana mining area, Ratnapura area, Sri Lanka	3.49 mm, GIA, A. Rajamanickam/V. Pardieu	$(Fe_{1.14}Mg_{1.75}Ca_{0.11}Mn_{0.01})[Al_{1.91}Fe^{3+}_{0.09}]Si_{3.00}O_{12}$
Pyrope GRR 749b	Anakapalle, Andhra Pradesh, India	1.09 mm, E. Grew; Geiger & Rossman (1994)	$(Mg_{1.69}Fe_{1.21}Ca_{0.08}Mn_{0.02})[Al_{1.99}Fe^{3+}_{0.03}]Si_{2.98}O_{12}$ - EMP
Pyrope GRR 131	unknown locality, East Africa Tanzania(?)	2.007 mm, Caltech Seismological Lab; Geiger & Rossman (1994)	$(Mg_{1.82}Fe_{0.98}Ca_{0.16}Mn_{0.04})Al_{2.00}Si_{2.99}O_{12}$ - EMP
Pyrope P-10	Ambodirafia, Madagascar	1.00 mm, MNHN 119.32; Geiger & Rossman (1994)	$(Mg_{1.47}Fe_{1.43}Mn_{0.02}Ca_{0.05})[Al_{2.12}Cr_{0.01}]Si_{2.96}O_{12}$

Pyrope GRR 779	Umba River Valley, Tanzania	0.79 mm, variety rhodolite; P. Flusser, Overland Gems; Geiger & Rossman (1994)	$(Mg_{1.61}Fe_{1.22}Mn_{0.04}Ca_{0.14})Al_{2.01}Si_{2.97}O_{12}$
Pyrope GRR 892	Himalaya Mountains, Nepal	A. Boettcher	$(Mg_{1.67}Fe_{1.14}Ca_{0.11})Al_{1.92}Si_{2.97}O_{12}$ - XRF
Pyrope 9093	Madagascar	1.06 mm, rhodolite; eBay	$(Fe_{1.08}Mg_{1.76}Ca_{0.11}Mn_{0.05})[Al_{1.92}Fe^{3+}_{0.08}Cr_{0.01}]Si_{3.00}O_{12}$
Pyrope 39060255315	Africa	1.56 mm, cut stone, eBay, labeled “Spessartine-Almandine”	$(Fe_{1.00}Mg_{1.75}Ca_{0.24}Mn_{0.02})[Al_{1.93}Fe^{3+}_{0.07}Ti_{0.01}]Si_{2.99}O_{12}$
Pyrope GRR 2268	Madagascar	1.54 mm, faceted gem, variety rhodolite; N. Brewer	$(Mg_{1.75}Fe_{1.04}Ca_{0.13}Mn_{0.06})Al_{1.98}Si_{3.01}O_{12}$
Pyrope GRR 2351	Kuranze - Kwale District Kenya	0.79 mm, rhodolite; J. Clanin	$(Mg_{1.77}Fe_{1.24}Mn_{0.03}Ca_{0.11})Al_{1.97}Si_{3.00}O_{12}$ - XRF
Pyrope GRR 83	Tanzania	0.78 mm, rhodolite; Pala International, Geiger & Rossman (1994)	$(Mg_{2.09}Fe_{0.78}Mn_{0.11}Ca_{0.11})[Al_{1.97}Cr_{0.02}]Si_{2.97}O_{12}$
Pyrope GRR 86	Tanzania	1.71 mm, rhodolite; Pala International	$(Mg_{1.1}Fe_{1.8}Mn_{0.07}Ca_{0.17})Al_{1.95}Si_{2.98}O_{12}$ - XRF
Pyrope 17405762	Turtle Land mine, Torapitiya area, Sri Lanka	4.32 mm, rhodolite; GIA, A. Konara/V. Pardieu	$(Mg_{2.19}Fe_{0.69}Ca_{0.13})[Al_{1.90}Fe^{3+}_{0.08}Cr_{0.01}Ti_{0.01}]Si_{3.00}O_{12}$
Pyrope 17405757	Rakwana mining area, Ratnapura area, Sri Lanka	2.95 mm, GIA, A. Rajamanickam/V. Pardieu	$(Mg_{2.12}Fe_{0.73}Ca_{0.11}Mn_{0.05})[Al_{1.90}Fe^{3+}_{0.09}Ti_{0.01}]Si_{3.00}O_{12}$
Pyrope 17405751	Gold mining area, Ruvu River, Matombo area, Tanzania	3.18 mm, GIA, V. Pardieu	$(Mg_{2.10}Fe_{0.67}Mn_{0.14}Ca_{0.10})[Al_{1.93}Fe^{3+}_{0.07}Cr_{0.01}]Si_{3.00}O_{12}$
Pyrope 17405770	Turtle Land mine, Torapitiya area, Sri Lanka	2.21 mm, rhodolite; GIA, A. Konara/V. Pardieu	$(Mg_{2.22}Fe_{0.65}Ca_{0.13})[Al_{1.86}Fe^{3+}_{0.12}Cr_{0.01}]Si_{3.00}O_{12}$

Pyrope SB #1	San Bernardo, Dora Maira, Italy	2.07 mm, light pink, Geiger & Rossman (1994; 2018)	$(Mg_{2.59}Fe_{0.35}Ca_{0.07})[Al_{1.97}Cr_{0.01}]Si_{3.01}O_{12}$
Pyrope SB #2	San Bernardo, Dora Maira, Italy	3.69 mm, dark pink, Geiger & Rossman (1994; 2018)	$(Mg_{2.54}Fe_{0.36}Ca_{0.09})[Al_{1.96}Fe^{3+}_{0.05}Cr_{0.01}]Si_{2.99}O_{12}$
Pyrope	Precise locality unknown, Dora Maira, Italy	2.96 mm, colorless, Geiger & Rossman (1994; 2018)	$(Mg_{2.95}Fe_{0.04}Mn_{0.01}Ca_{0.01})[Al_{1.99}Ti_{0.01}]Si_{2.99}O_{12}$

Table 1b. List and description of various natural almandine-spessartine garnets (only those samples listed in Table 2b were considered in the analysis of this work).

This is the peer-reviewed, final accepted version for American Mineralogist, published by the Mineralogical Society of America.
The published version is subject to change. Cite as Authors (Year) Title. American Mineralogist, in press.
DOI: https://doi.org/10.2138/am-2022-8499. http://www.minsocam.org/

Garnet Species & Sample Label	Locality	Sample Description	Composition
Almandine A-3	Roscoff, Sierck, Morbihan, France	0.75; MNHN (V), Pinet & Smith (1994); Geiger & Rossman (1994)	$(Fe_{2.06}Mn_{0.76}Mg_{0.08}Ca_{0.02})[Al_{2.05}Ti^{4+}_{0.01}]Si_{2.96}O_{12}$
Almandine A-20	Caladroy, Pyrénées-Orientales, France	1.01 mm; MNHN (V) 2448A; Pinet & Smith (1994); Geiger & Rossman (1994)	$(Fe_{2.11}Mn_{0.77}Mg_{0.08}Ca_{0.02})Al_{2.06}Si_{2.96}O_{12}$
Almandine GRR 3276	India (?)	0.50 mm & 0.213 mm; faceted dark purplish red gem; unknown jewelry dealer	$(Fe_{2.5}Mg_{0.3}Mn_{0.1}Ca_{0.1})Al_{2.0}Si_{3.0}O_{12}$
Almandine GRR 141	East Africa?	1.333 mm; vivid purplish red, E. Gaffney, Caltech Shockwave Lab; Geiger & Rossman (1994)	$(Fe_{1.42}Mn_{1.36}Ca_{0.03})Al_{2.01}Si_{2.99}O_{12}$
Almandine GRR 943	San Jacinto Mtn, Riverside County, CA, USA	2.70 mm; R. Hill, Caltech collection CIT-9968; Geiger & Rossman (1994)	$(Fe_{2.43}Ca_{0.16}Mn_{0.21}Mg_{0.09})Al_{2.01}Si_{3.00}O_{12}$
Spessartine Lind 2	Namibia	0.50 mm; Sps-Pyp, H. Lind	$(Mn_{2.44}Fe_{0.14}Mg_{0.37}Ca_{0.04})[Al_{1.99}Fe_{0.01}Ti_{0.01}]Si_{2.99}O_{12}$
Spessartine GRR 59b	Tanzania	Deep orange; Caltech Shockwave Lab; Geiger & Rossman (1994)	$(Mn_{1.72}Fe_{1.22}Ca_{0.02}Mg_{0.01})Al_{2.01}Si_{3.00}O_{12}$
Spessartine GRR 61	Brazil	1.35 mm; deep purplish red; Caltech Shockwave Lab Geiger & Rossman (1994)	$(Mn_{1.56}Fe_{1.38}Ca_{0.02})Al_{2.00}Si_{3.01}O_{12}$
Spessartine GRR 1052	Broken Hill, NSW, Australia	0.884 mm; deep reddish purple; Caltech collection CIT-11826	$(Mn_{2.04}Fe_{0.63}Ca_{0.37})[Al_{1.89}Fe_{0.13}Ti_{0.01}]Si_{2.99}O_{12}$ - XRF
Spessartine GRR 31	Minas Gerais, Brazil	0.905 mm; light orange; Caltech reference collection CIT-7765	$(Mn_{2.87}Fe_{0.10})Al_{1.96}Si_{3.00}O_{12}$ - XRF
Spessartine GRR 44B	Amelia, VA, USA	1.192 mm; grayish purplish red	$(Mn_{1.99}Fe_{0.88}Ca_{0.16})Al_{2.03}Si_{2.97}O_{12}$

		Caltech collection CIT-6725	
Spessartine GRR 1018	Rincon District, San Diego Co., CA, USA	1.145 mm; pegmatite district, Caltech collection CIT-15008; Geiger & Rossman (1994)	$(Mn_{1.35}Fe_{1.34}Mg_{0.09}Ca_{0.01})Al_{2.01}Si_{3.09}O_{12}$
Spessartine GRR 1041	Spruce Spine District, NC, USA	0.752 mm; dark reddish orange; Pegmatite, Caltech collection CIT-1738; Swanson & Veal (2010)	$(Mn_{1.64}Fe_{1.12}Mg_{0.03}Ca_{0.10})[Al_{1.95}Fe^{3+}_{0.05}]Si_{3.08}O_{12}$
Spessartine GRR 942	Ramona, CA, USA	0.696 mm; deep orange; M. Gray	$(Mn_{2.72}Fe_{0.24})Al_{1.98}Si_{3.00}O_{12}$ - XRF
Spessartine S-7	Chanteloube, Haute Vienne, France	MNHN (V), Pinet & Smith (1994)	$(Mn_{1.52}Fe_{1.44}Mg_{0.01}Ca_{0.02})Al_{1.98}Si_{3.00}O_{12}$ - XRF
Spessartine 370928271669 (316306)	Africa?	0.67 and 0.25 mm; cut crystal, ThaiGemStore; eBay	$(Mn_{2.30}Fe_{0.47}Mg_{0.15}Ca_{0.09})[Al_{1.97}Fe^{3+}_{0.02}Ti_{0.01}]$ $Si_{3.00}O_{12}$ - EDS
Spessartine S-14	Brasil	MNHN (V), Pinet & Smith (1994)	$(Mn_{1.86}Fe_{1.07}Ca_{0.06})Al_{2.00}Si_{3.00}O_{12}$
Spessartine GRR 2956	Little 3 Mine, near Ramona, San Diego Co., CA, USA	0.51 mm; M. Evans, Gemological Institute America, 3 to 5 mm crystals	$(Mn_{2.52}Fe_{0.45}Ca_{0.01})[Al_{2.03}Fe^{3+}_{0.01}]Si_{2.98}O_{12}$ - EDS
Spessartine GRR 72	Minas Gerais, Brazil	1.365 mm; purchased from Grieger's	$(Mn_{2.79}Fe_{0.07}Mg_{0.04}Ca_{0.08})Al_{2.06}Si_{3.05}O_{12}$
Spessartine GRR 43	Amelia, VA, USA	0.858 mm; light orange, Caltech collection	$(Mn_{2.82}Fe_{0.10})Al_{2.02}Si_{3.00}O_{12}$ - XRF
Spessartine MMUR 32999/912	Wushan Spessartine Mine, Fujian Province, PR. China	0.472 mm; orange, Boiocchi et al. (2012)	$\{Mn^{2+}_{2.87}Fe^{2+}_{0.09}Ca_{0.04}\}[Al_{1.94}Fe^{3+}_{0.06}](SiO_4)_{2.52}$ $(OH_{1.11},F_{0.81})$
Spessartine S-18	Tsilaisina, Madagascar	1.54 mm; MNHN 111.456; Pinet & Smith (1994)	$(Mn_{2.88}Fe_{0.04}Ca_{0.06})[Al_{1.95}Fe^{3+}_{0.05}]Si_{3.00}O_{12}$

809 [$]formula in this work is incorrect; MNHM - Muséum National d'Histoire Naturelle (V - Vésignié), Paris; GIA - Gemological Institute of America.

810

811

812

813

814

815

816

817

818

819

820

821 Supplementary Table 2a. Energies (in cm^{-1}) of various spin-forbidden Fe^{2+} (i.e., bands d, e, f, g, h, i, k, and q) and Fe^{3+} (i.e., bands l, m, and r)

822 transitions at room temperature for almandine-pyrope garnets (Table 1a) and their almandine mole fraction. Those samples shown in normal type

were measured in Kiev and those in italics in Pasadena. n.m. - not measured in UV region; n.d. - not determined (band too weak, broad or overlapped).

Sample/ Band	JF-1 Alm94	GRR 3276 Alm83	A-13 Alm81	*Jai-1* *Alm75*	GTF 90-28 Alm71	GRR 1056 Alm69	Lind 3 Alm69	P-10 Alm48	*GRR 779* *Alm41*	*GRR 749* *Alm40*
d	14320	14320	14330	14300	14340	14320	14310	14280	14380	14350
e	16260	16350	16330	16270	16340	16300	16270	16280	16280	16290
f	17460	17440	17440	17370	17410	17410	17350	17330	17410	17430
g	19170	19150	19080	19070	19090	19040	19060	19030	19130	19250
h	19760	19770	19760	19780	19780	19760	19760	19790	19820	19840
i	20090	20010	20060	20130	20080	20090	20010	20000	20170	20190
k	21600	21650	21610	21650	21690	21700	21620	21640	21750	21690
l	22750	22830	22940	22890	22900	n.d.	22820	22860	n.d.	n.d.
m	23090	23470	23360	23520	23460	23450	23410	23520	23550	23430
q	n.d.	24900	n.d.	25000	24910	25020	24910	25025	n.d.	n.d.
r	27050	27080	27100	n.m.	27080	27120	27130	27180	n.m.	n.m.

This is the peer-reviewed, final accepted version for American Mineralogist, published by the Mineralogical Society of America.
The published version is subject to change. Cite as Authors (Year) Title. American Mineralogist, in press.
DOI: https://doi.org/10.2138/am-2022-8499. http://www.minsocam.org/

826 Supplementary Table 2a (cont.).

Band	SM 1597 Alm39	Africa, …3845 Alm39	Africa, …9028 Alm39	Africa …8981 Alm39	*GRR 892 Alm39*	Rakwana 17405755 Alm38	*Rhodolite GRR 9093 Alm36*	GRR 2268 Alm35	*GRR 131 Alm33*	390602255315 Alm33
d	14270	14390	14490	14420	14360	14360	14310	14320	14340	14340
e	16180	16250	16300	16370	16270	16230	16230	16330	16290	16340
f	17340	17420	17510	17600	17400	17370	17390	17350	17400	17430
g	19070	19160	19180	19210	19130	19110	19080	19040	19090	19150
h	19780	19780	19790	19800	19830	19800	19800	19800	19790	19780
i	20110	20120	20070	20200	20080	20020	20080	20020	20150	20050
k	21640	21710	21760	21690	21690	21700	21680	21660	21730	21740
l	22900	n.d.	23010	n.d.	22890	22900	22880	n.d.	n.d.	n.d.
m	23470	23490	23390	23200	23510	23430	23470	23640	23730	n.d.
q	n.d.	n.d.	n.d.	n.d.	n.d.	n.d.	n.d.	n.d.	25210	n.d.
r	27210	27220	27130	27170	n.m.	27290	27210	27370	n.m.	27180

827

828 Supplementary Table 2a (cont.).

Band	*GRR 83* *Alm25*	Turtle Land Mine 17405762 Alm23	Rakwana 17405757 Alm23	Ruvu River 17405751 Alm22	Turtle Land Mine 17405770 Alm22	DM San Bernardo #1 Alm12	DM San Bernardo #2 Alm12	Dora Maira Colorless Alm1
d	14340	14330	14310	14330	14330	14240	14300	14220
e	16160	16270	16250	16210	16170	16170	16250	n.d.
f	17420	17360	17370	17370	17370	17320	17360	17300
g	19200	19060	19070	19050	19090	19110	19100	19070
h	19930	19820	19800	19820	19820	19820	19840	19850
i	20290	20080	20080	20040	20120	20100	20100	20150
k	21840	21710	21750	21730	21710	21670	21720	n.d.
l	n.d.	22940	n.d.	n.d.	22980	22940	22890	n.d.
m	23580	23580	n.d.	n.d.	23620	23630	23610	23620
q	n.d.	n.d.	n.d.	n.d.	n.d.	n.d.	25080	n.d.
r	27350	27300	n.d.	n.d.	27420	27360	27330	n.d.

829
830
831
832

This is the peer-reviewed, final accepted version for American Mineralogist, published by the Mineralogical Society of America.
The published version is subject to change. Cite as Authors (Year) Title. American Mineralogist, in press.
DOI: https://doi.org/10.2138/am-2022-8499. http://www.minsocam.org/

833 Supplementary Table 2b. Energies (in cm^{-1}) at room temperature of various spin-forbidden Fe^{2+} (i.e., bands d, e, f, g, h, i, j*, k, q),
834 Fe^{3+} (i.e., bands l, m, and r) and Mn^{2+} (i.e., bands n′, n, o, and p) transitions for almandine-(pyrope)-spessartine garnets (Table 1b)
835 and their almandine and spessartine mole fractions. Those samples shown in normal type were measured in Kiev and those in italics
836 in Pasadena. n.m. – not recorded in the UV region. n.d. – not detected (band too weak, broad or overlapped).

Band	JF-1 Alm94 Sps01	GRR 3276 Alm83 Sps03	A-13 Alm81 Sps08	A-3 Alm69 Sps25	*GRR 141* *Alm47* *Sps45*	*GRR 61* *Alm46* *Sps52*	*GRR 1041* *Alm37* *Sps55*	*GRR 44B* *Alm29* *Sps66*	*GRR 83* *Pyp70Alm26* *Sps04*
d	14320	14320	14330	14440	14420	n.m.	14550	n.d.	14240
e	16260	16350	16330	16300	16390	n.m.	16400	n.d.	16140
f	17460	17440	17440	17460	17560	17610	17700	17640	17390
g	19170	19150	19080	19100	19200	19150	19110	19080	19150
h	19760	19770	19760	19770	19790	19790	19810	19820	19920
i	20090	20010	20060	20050	20080	20060	n.d.	n.d.	n.d.
j	n.d.	n.d.	n.d.	n.d.	n.d.	n.d.	n.d.	20660	n.d.
k	21600	21650	21610	21620	21670	21700	21640	21700	21750
l	22750	22830	22940	n.d.	n.d.	n.d.	n.d.	n.d.	23200
m	23090	23470	23360	23430	n.d.	n.d.	n.d.	n.d.	23600
n′	n.d.	n.d.	n.d.	n.d.	n.d.	23320	23290	n.d.	n.d.
n	n.d.	n.d.	n.d.	23630	23630	23640	23560	23680	n.d.

o	n.d.	24150	24210	24250	24300	24320	24320	24390	24320
p	24660	24470	24490	24450	24520	24480	24500	24490	24590
q	n.d.	24900	n.d.	n.d.		n.d.	n.d.	n.d.	n.d.
r	27050	27080	27100	27110	n.m.	n.m.	n.m.	n.m.	27440

855 Supplementary Table 2b (continued).

Band	*GRR 1052* *Alm21* *Sps68*	316306 Alm16 Sps76	GRR 2956 Alm15 Sps85	271209132917 Alm08 Sps91	*GRR 942* *Alm08* *Sps91*	Lind 2 Alm5 Sps81	*GRR 31* *Alm03* *Sps96*	S-18 Alm01 Sps96
d	n.d.	n.d.	n.d.	n.d.	n.d.	n.d.	n.d.	n.d.
e	n.d.	n.d.	n.d.	n.d.	n.d.	n.d.	n.d.	n.d.
f	n.d.	n.d.	n.d.	n.d.	n.d.	n.d.	n.d.	n.d.
g	n.d.	n.d.	n.d.	n.d.	n.d.	n.d.	n.d.	n.d.
h	n.d.	n.d.	n.d.	n.d.	n.d.	n.d.	n.d.	n.d.
i	n.d.	n.d.	n.d.	n.d.	n.d.	n.d.	n.d.	n.d.
j	n.d.	n.d.	20670	20690	20700	20650	20680	20690
k	n.d.	n.d.	n.d.	n.d.	n.d.	n.d.	n.d.	n.d.
l	n.d.	n.d.	n.d.	n.d.	n.d.	n.d.	n.d.	n.d.
m	n.d.	n.d.	n.d.	n.d.	n.d.	n.d.	n.d.	n.d.
n′	23250	23190	23200	23200	23220	23140	23200	23200
n	23710	23670	23660	23650	23670	23630	23660	23670
o	24380	24240	24350	24310	24370	24250	24350	24350
p	24470	24390	24450	24450	24490	24420	24480	24450

q	n.d.	n.d.	n.d.	n.d.	n.d.	n.d.	n.d.	n.d.
r	n.m.	n.m.	n.d.	n.m.	n.m.	n.m.	n.m.	n.m.

868 **Figure Captions**

869

870 Figure 1a.) Polyhedral structure model of garnet. The tetrahedra and octahedra are connected
871 via shared corners and build a three-dimensional quasi framework. The X^{2+} cations (yellow
872 spheres) are located in small cavities of triangular dodecahedral coordination. The small red
873 spheres are oxygen ions and they lie on a single general crystallographic position *x*, *y*, *z*. b). A
874 central octahedron and six edge-shared dodecahedra (the polyhedral faces are shown as
875 concave to make the visualizing easier). c.) A central triangular dodecahedron and four edge-
876 shared octahedra. d). Edge-sharing relationship between neighboring triangular dodecahedra.

877 Figure 2. Stacked plot of eight almandine-pyrope garnet spectra with increasing almandine
878 content from bottom to top. The arrows indicate various spin-forbidden bands. The letters
879 follow the labelling of Moore and White (1972), as slightly modified by Taran et al. (Part II -
880 in press). The weak bands labeled p and o are related to Mn^{2+} and bands l, m and r are related
881 to Fe^{3+}. All other bands are due to Fe^{2+}. The "baseline" absorption increases with increasing
882 amandine (and Fe^{3+}) in the garnet because the O $\rightarrow$ M CT tail extends into the visible region.
883 The spectrum of almandine JF-1 (whose absorption is given by the ordinate on the right)
884 probably indicates the presence of a broad $^{VIII}Fe^{2+} + {}^{VI}Fe^{3+} \rightarrow {}^{VIII}Fe^{3+} + {}^{VI}Fe^{2+}$ IVCT band
885 centered roughly at 22,000 cm^{-1} (Geiger and Taran Part III - submitted). Its background is also
886 especially high because of the presence of numerous tiny solid inclusions scattered
887 throughout the crystal.

888 Figure 3. Energies for various spin-forbidden bands related to Fe^{2+} (solid circles) and Fe^{3+}
889 (solid squares) as a function of almandine mole percent (Supplementary Table 2a) for
890 almandine-pyrope solid solutions. The size of the symbols is larger than the experimental
891 uncertainty. The letters describe the various bands following Moore and White (1972), as

892 modified by this work and Taran et al. (Part II). The lines represent linear least-squares best
893 fits to the energies of the different bands.

894 Figure 4. Stacked plot of spectra of various almandine-spessartine garnets. Aside from the
895 spectrum of A-13, the spectra are shifted vertically for the sake of clarity. Note that the
896 absorption behavior for the spessartine-rich garnets is not a simple function of the spessartine
897 content. The arrows indicate several spin-forbidden bands related to Mn^{2+} and the letters
898 follow Moore and White (1972), as modified by Taran et al. (i.e., band n′ - Part II). The Mn^{2+}
899 band intensities are not a well-defined function of spessartine content in the garnet (see
900 discussion of this aspect in Part II).

901 Figure 5. Wavenumbers for spin-forbidden bands related to Fe^{2+} (solid circles) and Fe^{3+} (solid
902 squares) as a function of almandine mole percent (Supplementary Table 2b) for almandine-
903 spessartine solid solutions. The size of the symbols is larger than the experimental
904 uncertainty. The lines represent linear least-squares best fits to the energies for a number of
905 lower energy bands. No fits were made to the energies of the three highest energy bands
906 because of the limited data coverage.

907 Figure 6. Wavenumbers for the most intense spin-forbidden bands related to Mn^{2+} lying
908 between 23000 and 25000 cm^{-1} (n′, n, o and p) as a function spessartine mole percent in the
909 garnet (Supplementary Table 2b) for almandine-spessartine solid solutions. The size of the
910 symbols is larger than the experimental uncertainty. The lines represent linear least-squares
911 best fits to the energies of the different bands.

912

913

914

This is the peer-reviewed, final accepted version for American Mineralogist, published by the Mineralogical Society of America.
The published version is subject to change. Cite as Authors (Year) Title. American Mineralogist, in press.
DOI: https://doi.org/10.2138/am-2022-8499. http://www.minsocam.org/

915

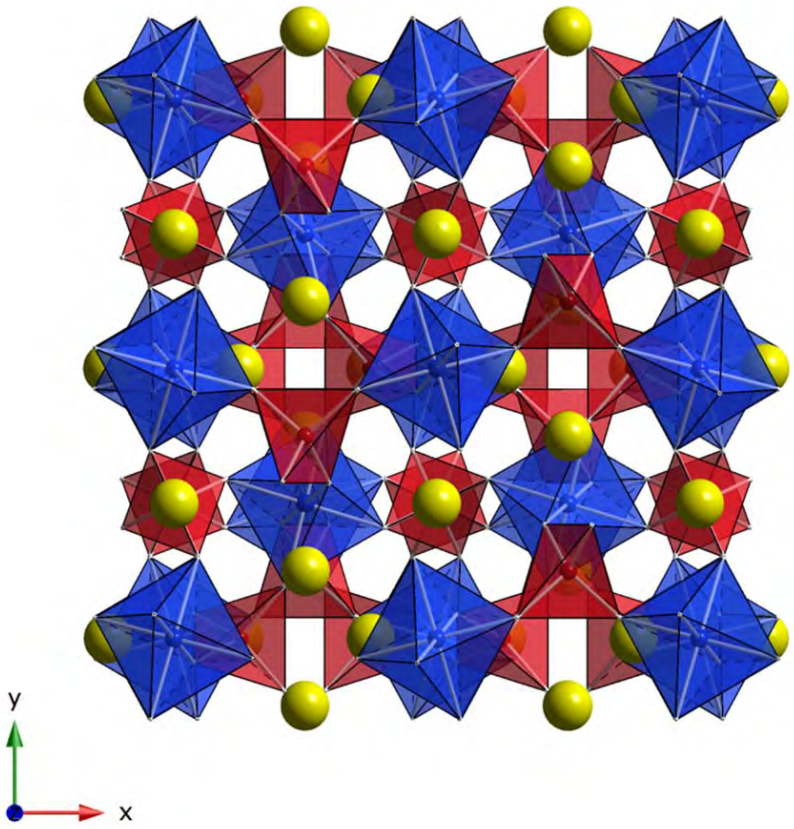

916

917 a.)

918

919

920

This is the peer-reviewed, final accepted version for American Mineralogist, published by the Mineralogical Society of America.
The published version is subject to change. Cite as Authors (Year) Title. American Mineralogist, in press.
DOI: https://doi.org/10.2138/am-2022-8499. http://www.minsocam.org/

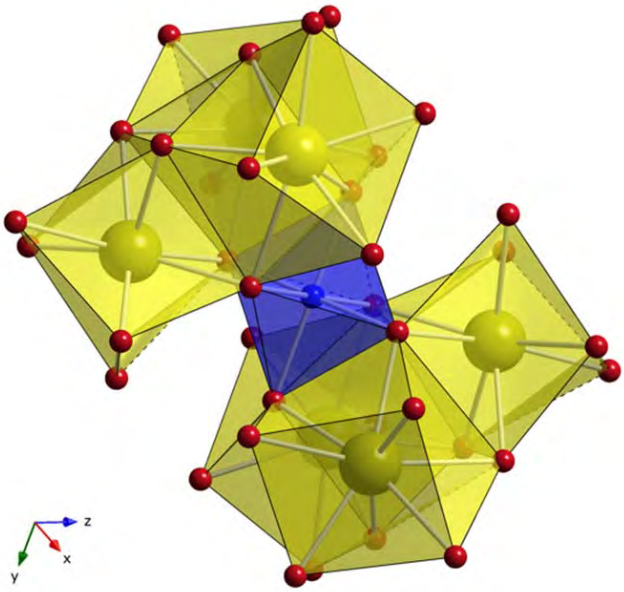

b.)

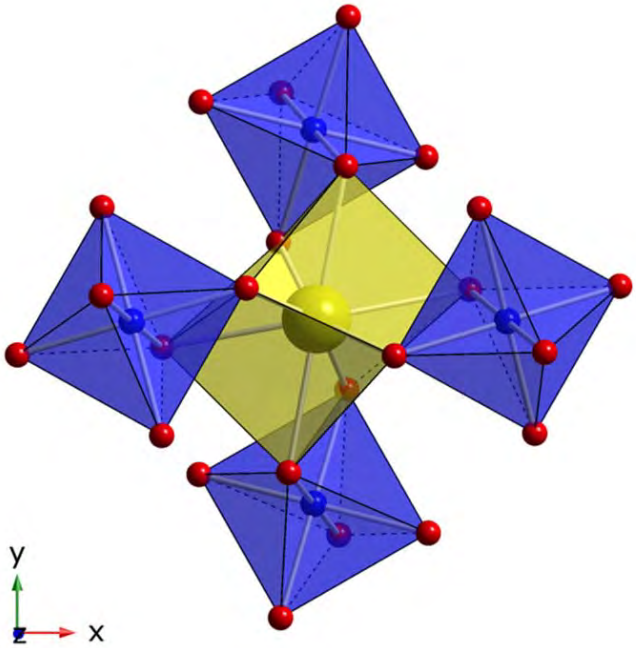

c.)

This is the peer-reviewed, final accepted version for American Mineralogist, published by the Mineralogical Society of America.
The published version is subject to change. Cite as Authors (Year) Title. American Mineralogist, in press.
DOI: https://doi.org/10.2138/am-2022-8499. http://www.minsocam.org/

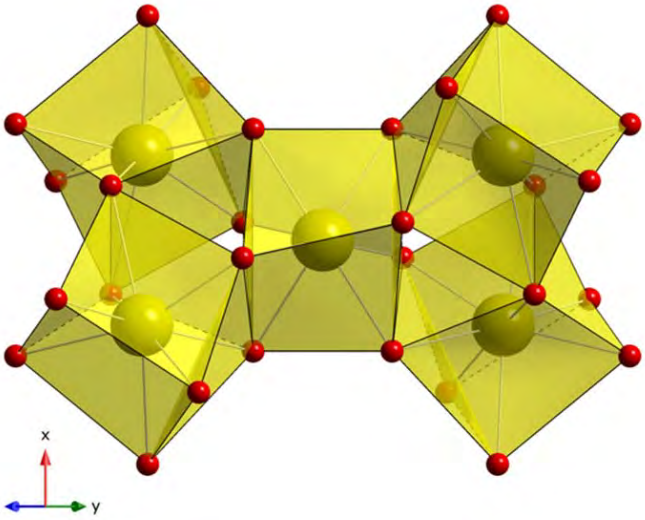

d.)

Figure 1.

This is the peer-reviewed, final accepted version for American Mineralogist, published by the Mineralogical Society of America.
The published version is subject to change. Cite as Authors (Year) Title. American Mineralogist, in press.
DOI: https://doi.org/10.2138/am-2022-8499. http://www.minsocam.org/

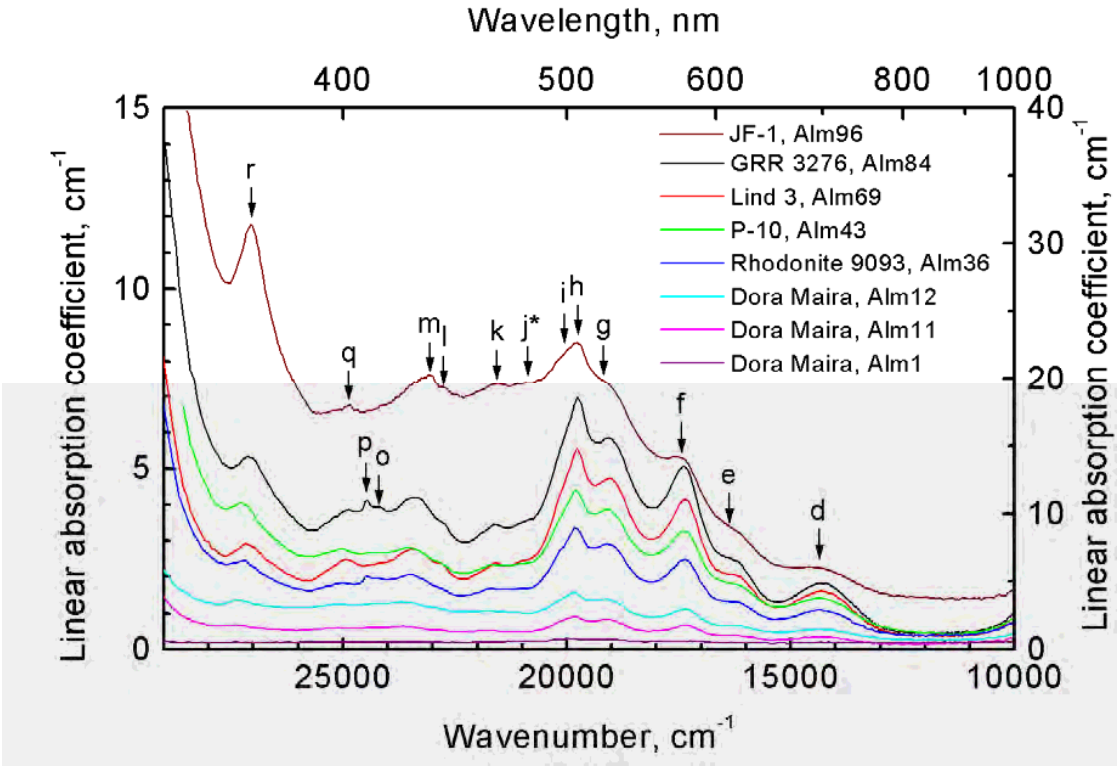

Figure 2.

974

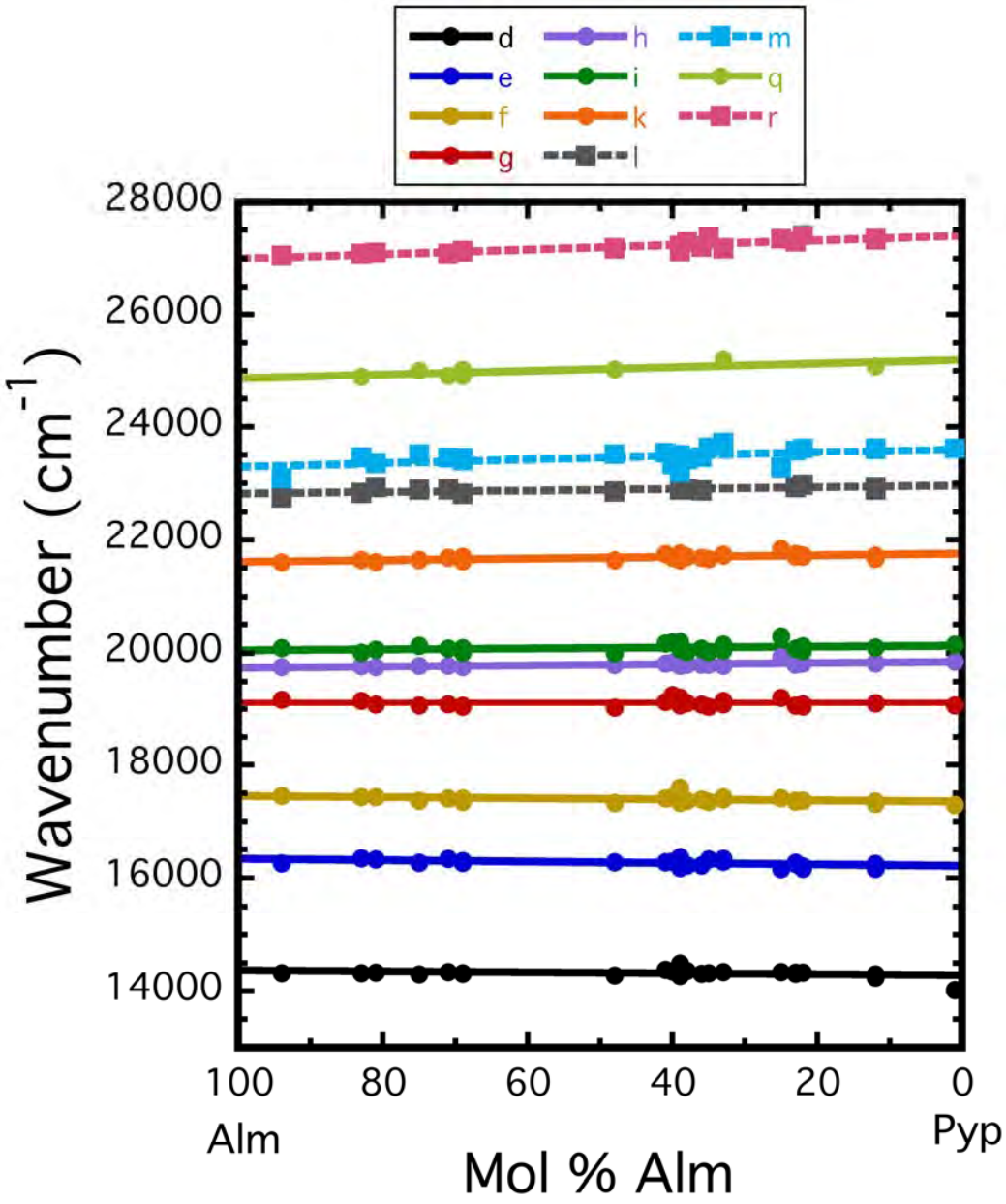

975
976
977
978
979 Figure 3.
980
981
982
983

This is the peer-reviewed, final accepted version for American Mineralogist, published by the Mineralogical Society of America.
The published version is subject to change. Cite as Authors (Year) Title. American Mineralogist, in press.
DOI: https://doi.org/10.2138/am-2022-8499. http://www.minsocam.org/

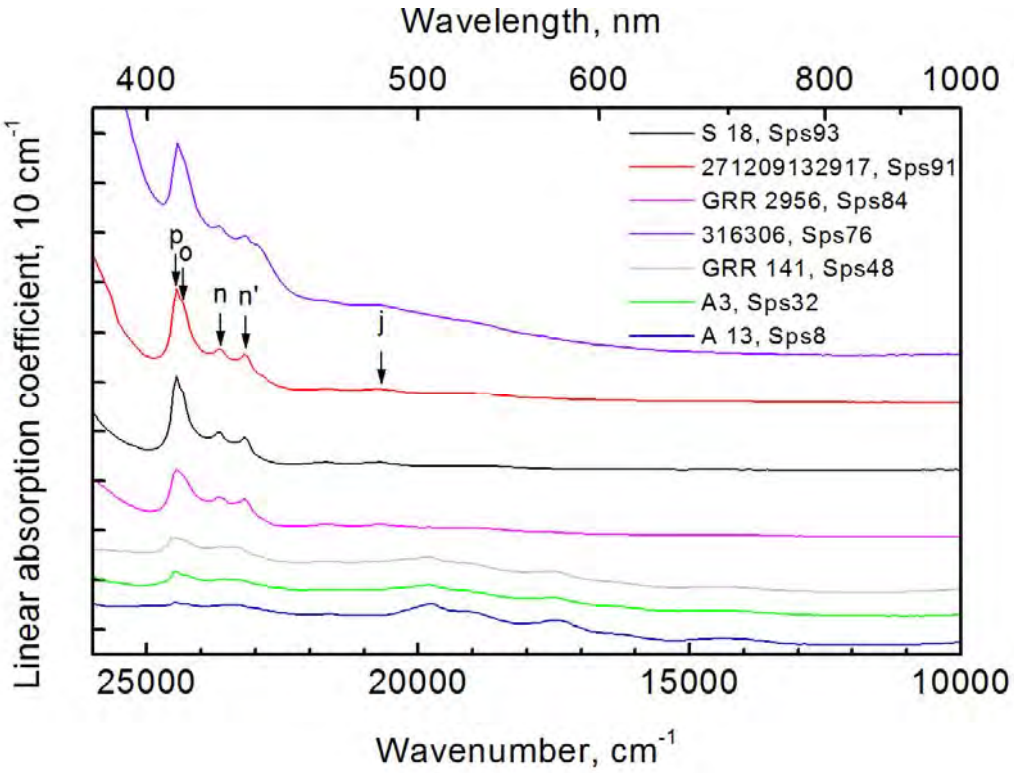

Figure 4.

This is the peer-reviewed, final accepted version for American Mineralogist, published by the Mineralogical Society of America.
The published version is subject to change. Cite as Authors (Year) Title. American Mineralogist, in press.
DOI: https://doi.org/10.2138/am-2022-8499. http://www.minsocam.org/

1005

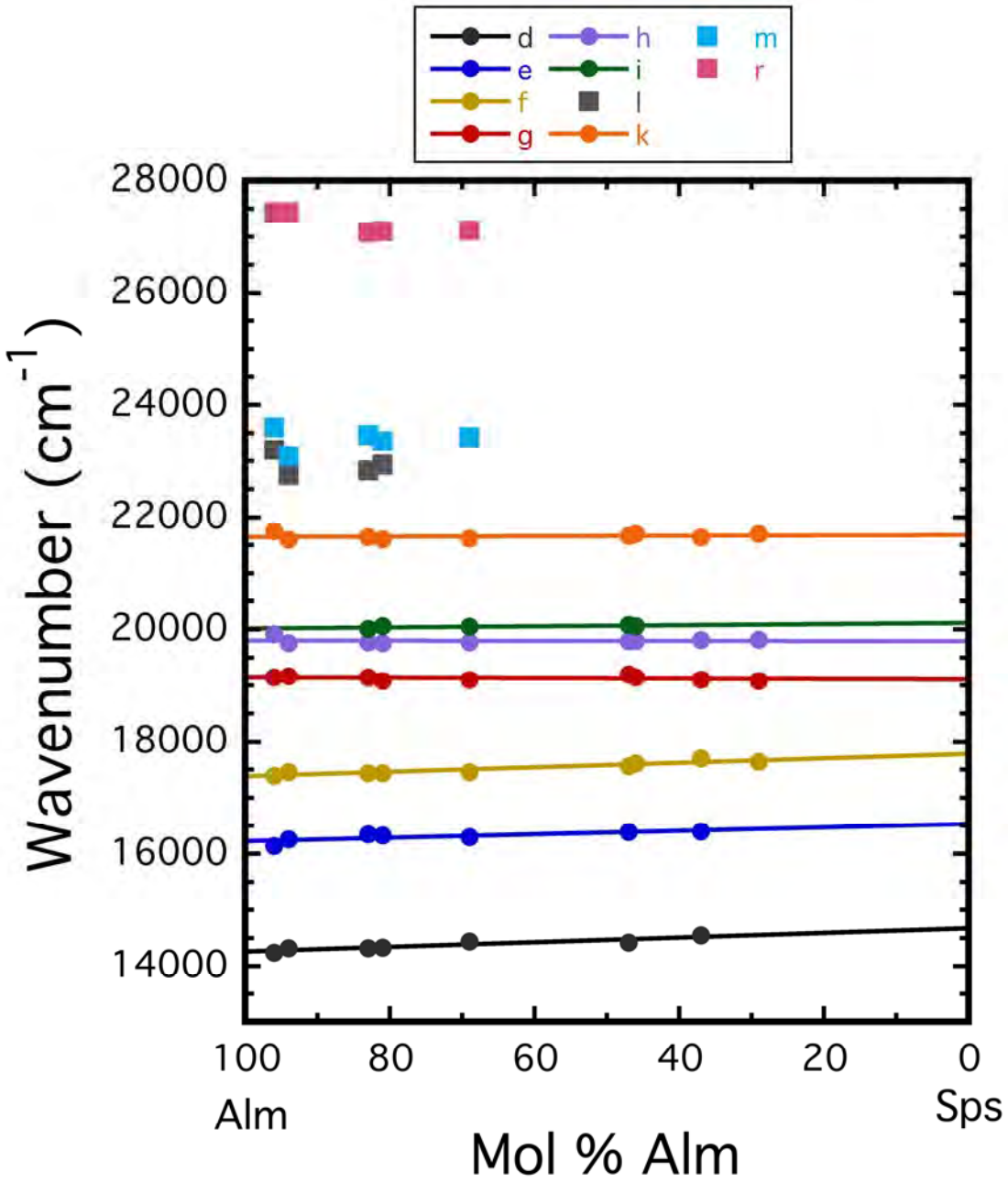

1006

1007

1008 Figure 5.

1009

1010

1011

1012

1013

This is the peer-reviewed, final accepted version for American Mineralogist, published by the Mineralogical Society of America.
The published version is subject to change. Cite as Authors (Year) Title. American Mineralogist, in press.
DOI: https://doi.org/10.2138/am-2022-8499. http://www.minsocam.org/

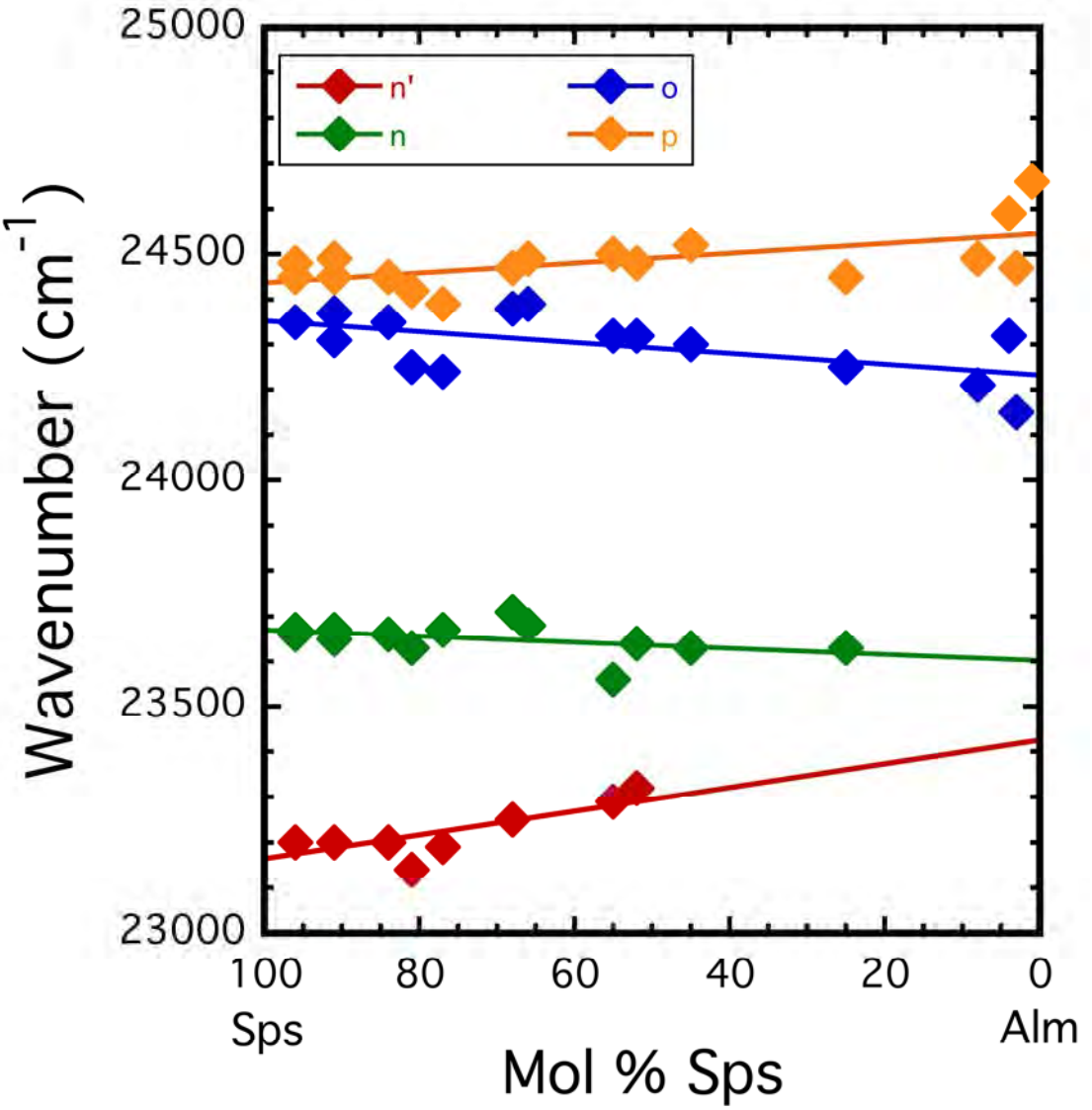

1014

1015

1016

1017

1018

1019 Figure 6.